POLITECNICO DI TORINO

Master of Science in Energy and Nuclear Engineering

Master of Science Thesis

Analysis of different options for the cooling of in-vessel components in DEMO fusion reactor

Supervisor:
Dr. Antonio Froio
Co-supervisors:
Dott. Andrea Zapppatore
Prof. Roberto Zanino

Candidate:
Nicolò Garelli

Accademic Year 2020-2021

This page is intentionally left blank.

Abstract

The present work investigates the time to cool down a Water-Cooled Lithium-Lead (WCLL) Breeding Blanket (BB) sector of the EU DEMO fusion reactor, starting from the after-shutdown condition of 300°C towards the prescribed temperature for Remote Maintenance (RM) operations, 150°C.

First part of the analysis foresees air in natural convection as cooling medium. Weighted solid properties and decay heat load of WCLL have been evaluated and implemented in a 3D transient conjugate heat transfer model, already developed for HCPB BB concept. Comparison between the two concepts is carried out.

Air in forced convection is the second investigated cooling strategy. The previous 3D model has been properly modified to take into account the presence of turbulence, which significantly rises the complexity of the problem. Two simpler 2D model problems have been solved and adopted to make the right choice on turbulence model and meshing strategy for the complex 3D setup. The first 2D model studies turbulence inside a narrow rectangular duct, which has the same width of the small gaps between adjacent BB segments. Nusselt number found numerically has been compared with correlations for turbulent flow available in literature, Reynolds number ranging from Re=12000 to Re=51000. Once assessed the agreement between the two, a second model problem has been developed to study the abrupt area contraction experienced by air which enters small gaps coming from the equatorial port, the prescribed air inlet. Nusselt number has been evaluated to ensure agreement with the previous cases whereas localized contraction coefficient has been compared with literature values to assess the goodness of the model in this critical location. The selected meshing strategy and turbulence model have been adopted in the full 3D model, even if some adjustments have been necessary to reduce the cells count, which, in the worst case, goes up to $\sim$ 30 millions. The results in forced convection are then compared against those obtained in natural convection.

Acknowledgements

Computational resources provided by hpc@polito, which is a project of Academic Computing within the Department of Control and Computer Engineering at the Politecnico di Torino (http://www.hpc.polito.it).

Ringrazio i miei supervisori, in particolare Antonio Froio e Andrea Zappatore, per avermi guidato con disponibilità e pazienza durante la realizzazione di questo lavoro, nonostante le difficoltà incontrate.

Ringrazio sentitamente i miei genitori, per avermi lasciato la libertà di decidere ogni passo del mio percorso accademico, condividendo le mie scelte e sostenendole economicamente. Senza di voi questo traguardo non sarebbe stato possibile. Una menzione particolare va a mio fratello Mattia, fedele compagno durante i momenti di svago casalinghi, sopratutto nei mesi più difficili della pandemia.

Grazie alla mia fidanzata Federica, a cui numerose volte ho affidato le mie preoccupazioni ricevendo costante sotegno.

Ringrazio infine gli amici con cui ho condiviso questo percorso, a partire dalle ore di lezione e quelle a studiare o scrivere relazioni, per finire con le pause pranzo in mensa e i numerosi momenti fuori dall'università. Se avrò sempre un bellissimo ricordo del periodo universitario e della vita torinese, il merito è soprattutto vostro.

Nicolò

Contents

List of Figures

List of Tables

Chapter 1

Introduction

1.1 Nuclear fusion

Nuclear fusion is perhaps the most promising way to produce energy in large amount, in an environmentally friendly way without relying on an unpredictable (or at least discontinuous) energy source as wind or sun. It exploits exothermic nuclear reactions in which two reactant merge together to create a heavier nucleus (and other products). The most promising fusion reaction on Earth involves two Hydrogen isotopes, Deuterium and Tritium, and produces a nucleus of Helium together with a single isolated neutron (see equation 1.1).

$$ {}^{2}_{1}\mathrm{H} + {}^{3}_{1}\mathrm{H} \longrightarrow {}^{4}_{2}\mathrm{He} + {}^{1}_{0}\mathrm{n} + 17.59\,\mathrm{MeV} \tag{1.1} $$

In order to have a sufficient amount of fusion reactions, extremely high temperature of the Deuterium-Tritium mixture is required inside a fusion reactor. They reach temperatures in the order of 100 million Kelvin, where matter is in the plasma state, materials are partially or fully ionized and electrons and ions are freer to move. These few pieces of information already give an idea of the complexity of the physics and engineering behind nuclear fusion and this is the reason why it is still a really challenging research field and not yet a solution to produce energy on a large scale.

Magnetic confinement is adopted to keep plasma in a controlled environment because, at those temperatures, it cannot be in contact with other materials, otherwise it would melt them in less than few seconds. Although there are also other confinement options, tokamak is surely the most widespread configuration among both the already built fusion devices (just research facilities) and the current projects for future reactors. It foresees the confinement in a donut-shaped space (called torus) thanks to a combination of three different magnetic field:

- *Toroidal field*: produced by a set of toroidal coils spaced around the torus.

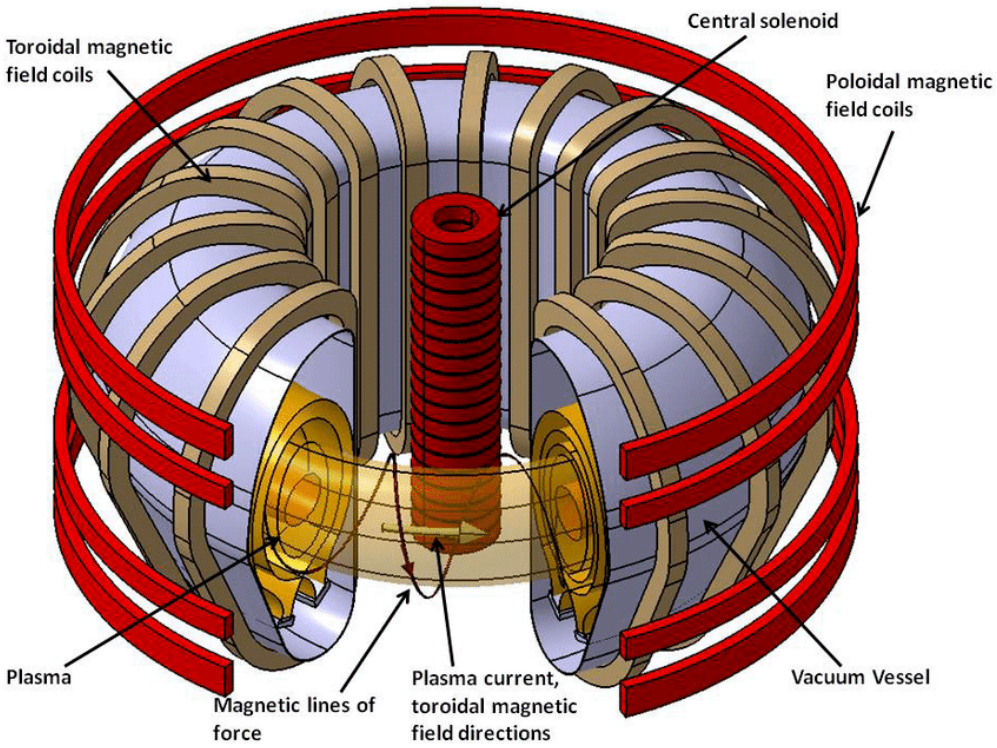

Figure 1.1: Tokamak schematic with magnetic field coils [1].

This is a discrete approximation of the standard solenoid, designed to get the best magnetic field while leaving space to access the plasma chamber. This field is mainly useful to ensure stability of the equilibrium inside plasma and it is generated by Ampere's law from a direct current.

- *Poloidal field*: produced by the current circulating inside the plasma. This is the most delicate one because generated mainly inductively. Starting from a pulsed current in the central solenoid, exploiting the transformer principle, a current is generated inside plasma. In turn, thanks to Ampere's law, it will generate a poloidal magnetic field whose primary function is plasma confinement.

- *Vertical field*: produced by a set of poloidal coils. It is useful to control the shape of the field according to the phase of the plasma discharge. Again created by Ampere's law, here with a time dependent current inside coils, because this field is always changing in time.

In order to keep the confined environment at these extremely high temperature, a self-sustained process inside plasma chamber should be obtained. Indeed, Every He

nucleus (also called α particle) produced in a D-T reaction takes approximately one fifth of the total energy released (one fifth of 17.59 MeV $\simeq$ 3.5 MeV), which means its energy is more than 100 times higher than the average energy of a particle inside plasma (equation 1.2 shows the conversion between K and temperature expressed in energy units, widely used in fusion field). Thanks to scattering, α particles are able to spread energy inside plasma. If this process reaches the right extent, plasma will be warm enough to make other fusion reactions and keep the heating inside the reactor. However, there are still several difficulties in both establishing this configuration and keeping it for a sufficient time.

$$100 \times 10^6\,\mathrm{K} = \frac{100 \times 10^6\,\mathrm{K} \cdot k_B}{1.6022 \times 10^{-13}\,\mathrm{J\,MeV^{-1}}} \simeq 1 \times 10^{-2}\,\mathrm{MeV} \tag{1.2}$$

where $k_B = 1.380\,649 \times 10^{-23}\,\mathrm{J\,K^{-1}}$ is the Boltzmann constant.

Currently, there are two main projects under development concerning nuclear fusion:

- *ITER* this is the most mature project, a research reactor actually under construction in France and result of international joint experiment with 35 nations involved. It aims to produce for the first time net energy via fusion reaction and to maintain fusion reaction for long time. The first plasma is scheduled for December 2025. The long-term purpose of ITER is the study of plasma under conditions similar to those expected in a large scale fusion reactor for electricity production [2].
- *DEMO* the last evolution of ITER project, DEMO aims to be the final step before commercial power plants. Planned to be constructed around 2050, the project managed by EUROfusion organization is currently in early design stage. The main DEMO objective is the production of electricity, although not in large quantities [3].

1.2 Tokamak key challenges in DEMO perspective

Three fundamental challenges must be overcome in order to produce electricity through fusion reactors:

- "Managing the power and particles exhaust from the plasma, while controlling impurities production inside plasma chamber" [4];
- "Extracting the power deposited in the blanket by the neutrons, while breeding the tritium fuel and shielding the superconducting magnets" [4];

- "Confining a 100 million K plasma using powerful superconducting magnets, while keeping them at 4.5 K" [4].

1.2.1 Power exhaust

As mentioned before, the fusion reaction creates two products, α particles and neutrons. Neutrons, due to their neutrality, are not influenced by magnetic field and have the capability to penetrate materials, reason why they are associated to power extraction issue. α particles, instead, are magnetically confined and deposit power inside plasma, which must be exhausted by one of the three standard propagation mode: conduction, convection and radiation. The intrinsic anisotropy of the last two ways raises the first issue: the exhaust of power through conduction and convection is more effective along magnetic field line direction (because the anisotropy is associated to motion) and the cooling area, which could be the total surface of the torus, is significantly reduced. There will be portion of the First Wall (the innermost layer of material inside the toroidal chamber) much more stressed than other and not able to withstand such a power. In this already difficult situation, plasma-surface interactions (PSI) further complicate the game. Introduction of impurities inside plasma occurs after interaction between D and T ions and First Wall. Since it is not possible to reach perfect magnetic confinement, sooner or later there will be some interactions between the two and this phenomenon can cause the reactor to be turned-off because of line radiations.

One revolutionary idea to solve this problem has been the Divertor idea. As said, it is not possible to get perfect confinement, therefore plasma chamber can be divided in two parts:

- *Core Plasma*: the innermost portion of the chameber, where magnetic field lines are closed and plasma does not see solid surfaces.
- *Scrape-Off Layer (SOL)*: the outer region where magnetic field lines are cross solid surfaces of first wall and plasma is going to interact with them.

The two portions are splitted by the Separatrix or Last Closed (Magnetic) Flux Surface (LCFS). In divertor configuration, another magnetic coil is added in toroidal direction: the current flows in the same direction of plasma current and it makes another poloidal field. The superposition of the two poloidal fields creates a X-point (in which the poloidal field is null) and this new configuration brings SOL magnetic field lines to be diverted in the bottom part of the plasma chamber, where they find two solid component called divertor plates. This complex solution is useful to increase the distance between the core plasma and the impurities and it was found to be really effective compared to previous adopted solution. The divertor configuration has already been implemented in past reactors, it is foreseen for

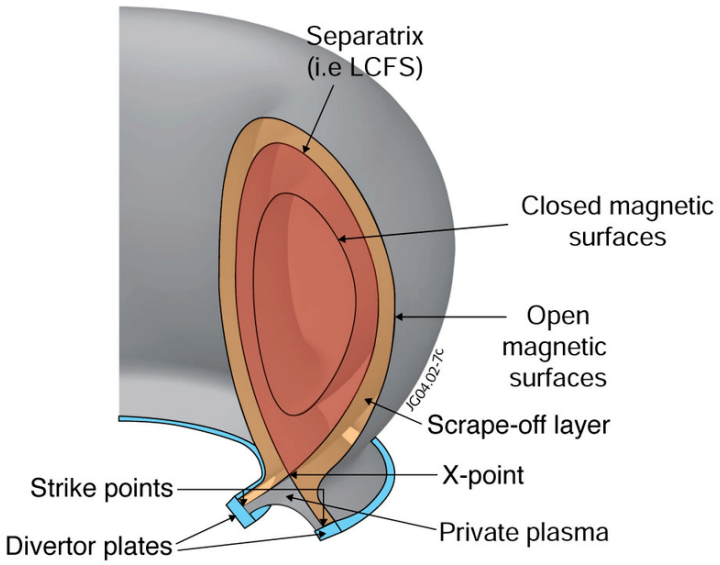

Figure 1.2: Sketch of Tokamak Divertor configuration [5].

ITER and it will be present also in DEMO. However, due to the increasing complexity of the devices, several studies are necessary to improve its performances. Starting from the solid Tungsten divertor designed for ITER, the research is going towards advanced divertor such as Liquid Metal divertor and complex magnetic configuration in order to withstand the higher heat loads of DEMO. in figure 1.2 is shown an example of divertor type Tokamak.

1.2.2 Cooling Magnets

The magnetic fields needed to confine plasma are extremely high in terms of magnitude: ITER toroidal field coils are designed to produce a maximum magnetic field of 11.8 T [2]. Currents inside these magnets are the highest ever produced. In this framework, superconductors are necessary otherwise Joule losses would be higher than the power produced by the reactor itself. At present, the main interest is towards Low Temperature Superconductors (LSC), whereas high temperature ones are still a more advanced solution. However, in both cases, a very powerful cryogenic facility is needed to get low resistivity inside superconductors. When the temperature limit is exceeded, resistivity rises very fast and superconductivity is lost. Niobium Titanium ($NbTi$) and Nb_3Sn are the most common superconducting materials used in fusion, the latter has the best performances. Forced flow cooling of supercritical He is adopted in the majority of fusion devices, ITER included, to keep the 4.5 K designed temperature for operation. It would not be

possible to maintain this temperature without breeding blanket and vacuum vessel shielding, which limits in large extent the magnets heating caused by neutrons.

1.2.3 Breeding Blanket

The blanket is one of the key components of a fusion reactor. ITER will be the first reactor equipped with a blanket, even if not a breeding one. On the other hand, DEMO should necessarily be provided with a breeding blanket, otherwise it will not be possible to meet its goals. A breeding blanket performs three main functions:

- *Extracts the power deposited by neutrons.* High energetic neutrons coming from the plasma are not influenced by the magnetic field and penetrate the first wall. Interacting with solid walls, they release their energy, which is taken away by a coolant.

- *Breeds and extracts tritium fuel.* Tritium is radioactive with a quite short half life (12.3 years), therefore it is not available in nature. Apart from Pressurized Heavy Water Reactors (like CANDUs), in which tritium is produced as waste, there is no tritium external source available for fusion reactors. Moreover, the tritium production of the whole CANDU fleet will not be sufficient to feed even just one fusion power plant. This scenario brings the need to implement a breeding technology inside commercial fusion reactors. The easiest way to breed tritium is to start from lithium (Li) because it is abundant on earth and it reacts with a neutron to get T and other products. The tritium produced inside blanket is then extracted by tritium extraction/removal system and inserted in the plasma chamber together with Deuterium.

- *Shields magnets.* As mentioned before, plasma temperature reaches incredibly high values. On the other hand, magnets employed to confine plasma must be kept at really low temperatures, otherwise their performances would suffer a substantial deterioration. Breeding blanket, together with the vacuum vessel located right onwards, have the function to shield neutrons from magnets, since they are highly energetic and they will heat them up.

Currently, multiple breeding blanket concepts have been developed, using very different technologies. The most promising solutions will be tested in ITER via Test Blanket Modules (TBM) project, where breeding blanket tiles will be inserted in the plasma chamber in order to study their performances during operation. The full implementation of a breeding blanket is foreseen in DEMO for the first time. For this reason, multiple issues still have to be solved to get the final version. At

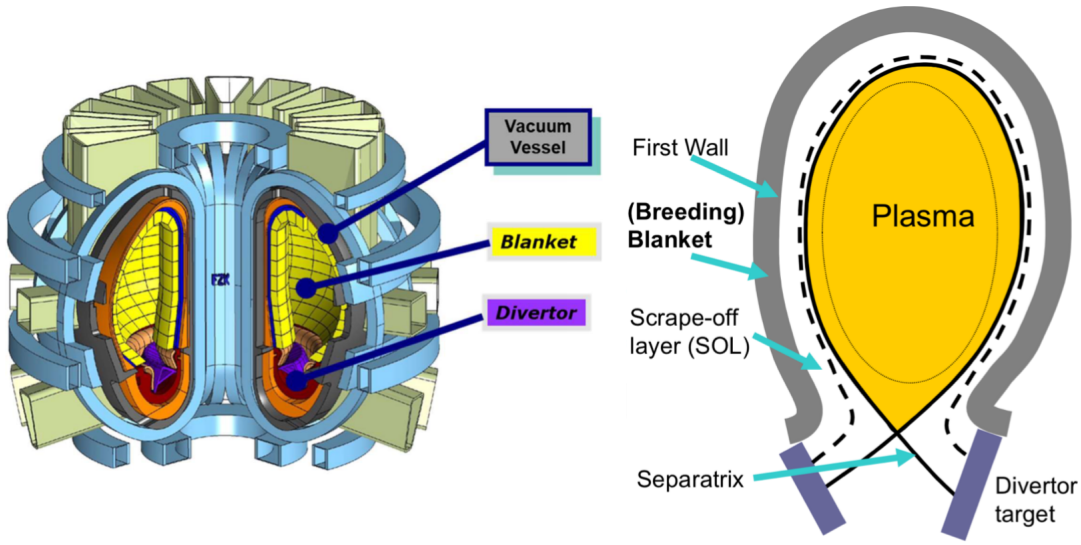

Figure 1.3: Breeding Blanket position in Tokamak (left) and details about plasma regions (right) [6].

present, two solution are considered particularly promising by European scientists :

- *Helium Cooled Pebble Bed (HCPB)*: solid Li breeder, Beryllium to multiply neutrons via $(n, 2n)$ reaction, Helium coolant. EUROFER as structural material. Solid breeder organized in pebbles, tritium extraction via purged gas [7].
- *Water Cooled Lithium Lead (WCLL)*: eutectic PbLi as liquid breeder which acts also as multiplier (Pb in this case), cooled by water. EUROFER as structural material. Permeation Against Vacuum (PAV) technology to extract tritium from liquid breeder [8].

Both these solution will be tested in ITER TBM project. In figure 1.4 is shown an example of breeding blanket promising solution.

1.3 DEMO BB segments Remote Maintenance

1.3.1 Problem description

Materials degradation by neutron irradiation is a key issue in fusion reactor design. On the one hand, expecially in future reactors, designed to produce electricity,

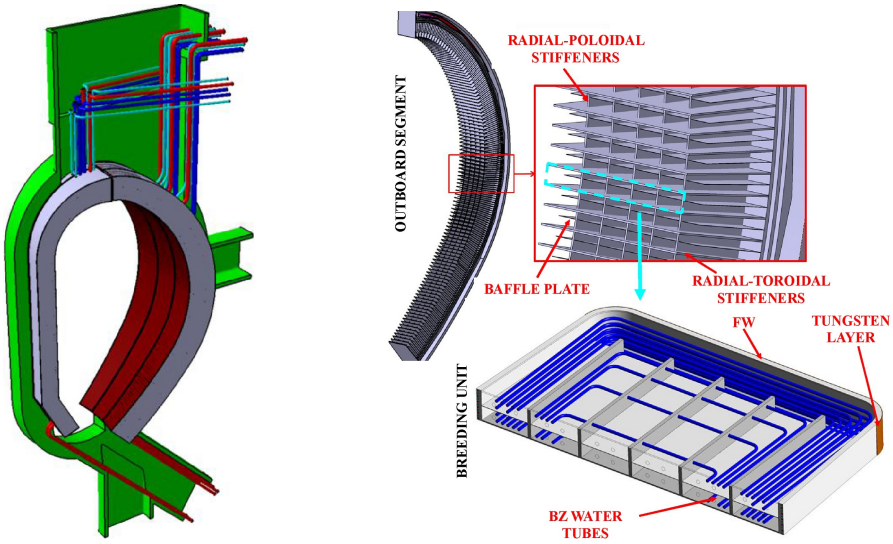

(a) DEMO WCLL BB system with PbLi and coolant systems [9].

(b) WCLL BB 2016 design: outboard segment and breeding unit at equatorial plane [9].

Figure 1.4: WCLL BB concept 2016 version.

availability must be fully maximized. On the other, some components need periodic maintenance otherwise structural material performances would be strongly weakened by irradiation (First Wall could get more than 800 displacements per atom (dpa) in a standard European fusion power plant [10]). Figure 1.5 shows the components subject to replacement during power plant lifetime. In DEMO, all breeding blanket segments will be replaced and maintenance time should not overcome a certain threshold in order to meet DEMO availability targets [12]. Moreover, failure of in-vessel components (IVCs) cannot be excluded and replacement of individual BB segments must be feasible [12]. Due to the irradiation levels reached by components inside the reactor, Remote Maintenance technologies will be necessarily used to perform this task, otherwise operators will face unacceptable irradiation doses.

More than one solution have been investigated to solve RM issue. Among them, vertical maintenance Remote Handling (RH) system for multi module blanket segment is one of the most interesting. This design foresees BB segments removal via the torus upper vertical port, visible in figure 1.6. Due to space limitation between toroidal field coils, the upper port has limited dimension. For this reason, every blanket sector is divided in two inboard segments and three outboard segments. This is the best solution to make possible remote handling from upper port while decreasing as much as possible the removal time. However, the small difference between upper port and BB segments dimensions makes RM a really challenging

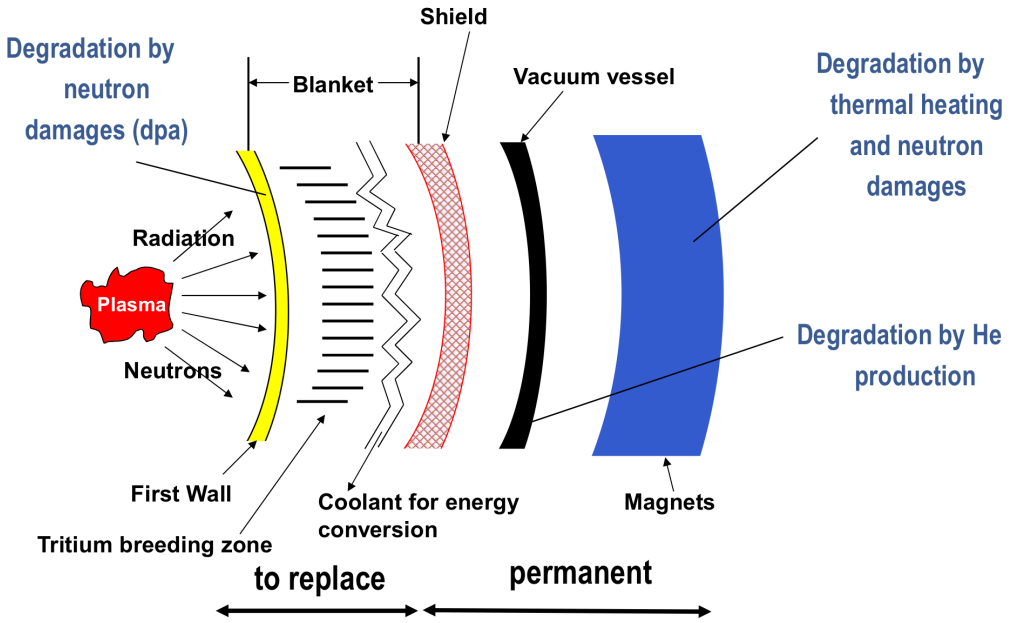

Figure 1.5: DEMO components lifetime [6].

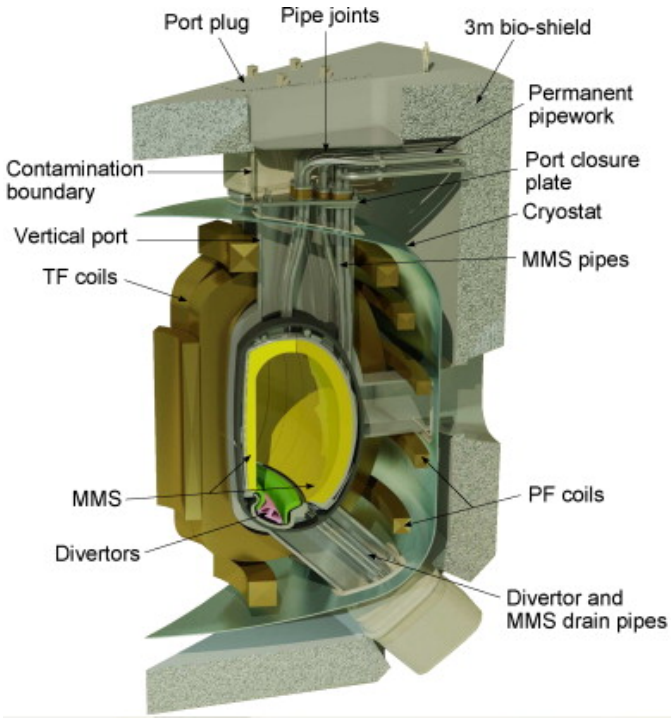

Figure 1.6: DEMO vertical upper port geometry and blanket modules service connections [11].

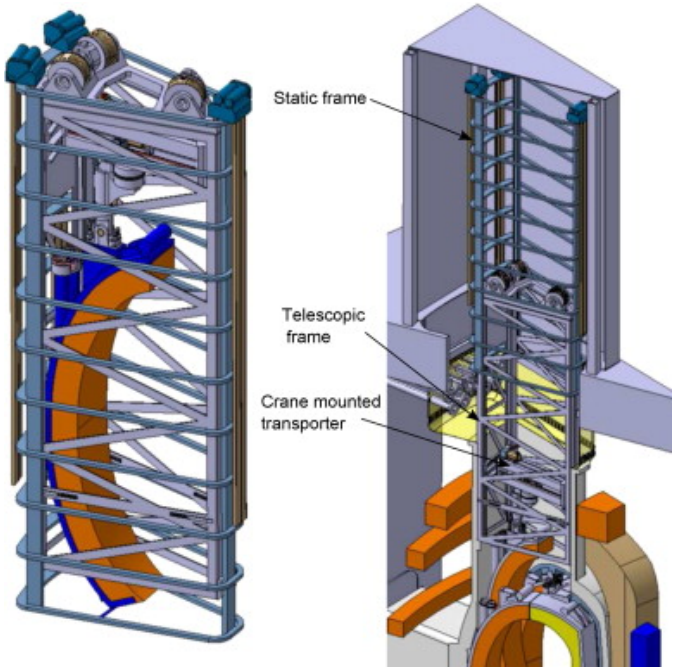

Figure 1.7: Fully retracted Vertical Maintenance Scheme with central OB segment (left) and extended Vertical Maintenance Crane (right) [11].

operation. Indeed, every BB segment is extracted in precise order and complex manipulation is required for inboard ones to get the right position before lifting operations. It is worth mentioning also access port opening and closing procedures: dedicated equipments are employed for service connection rupture and vacuum port closure removal. In particular, Pipe Joint Cask (PJC) operations to remove and install all the pipe joints takes approximately 60% of the total estimated duration of maintenance operation [11]. The Vertical Maintenance Scheme (VMS) should be able to complete full blanket and divertor replacement in approximately 6 months [11]. In figure 1.7 is shown the lifting installation placed after the pipe cutting and closure removal.

1.3.2 Aim of the work

Regardless the RM technology, operational requirements for RM robots are very strict, considering the extreme precision required during large and massive objects handling in narrow spaces. One of such requirements is the temperature of the handled item, which, for BB maintenance, must be below 150°C [13]. The aim of the present work is the simulation of BB cooling transient to reach 150°C for the RM operations, considering as initial condition the operating temperature of

$\simeq$ 300°C. Starting from the study carried out for HCPB [7] BB concept in case of natural convection cooling [14], the present work will evaluate the cooling time for WCLL [8] BB concept in both natural and forced convection strategies, using 3D Computational Fluid Dynamics(CFD) models to simulate the Conjugate Heat Transfer (CHT) problem at hand. The results will be useful to compare the two most promising BB technologies from maintenance point of view and they will be part of the overall discussion to get the best DEMO BB technology.

Chapter 2

Natural Convection Study

First analysis of the present work is performed considering WCLL BB concept cooled down by external air flow in natural convection. Cooling must be provided by an external media because active cooling is no longer available to let the RM systems access the sector segment. The selected WCLL BB concept is taken from *WCLL Design Report* [15]. It is possible to exploit the CFD setup already implemented for HCPB BB concept with air in natural convection [14]. However, due to the blanket concept change, preliminary calculations of BB thermophysical properties and heat load caused by neutron activation are required. This first assessment will provide a rough estimation of cooling time in case of WCLL BB concept, useful to make predictions in view of more complex calculations involving turbulence.

2.1 WCLL Thermophysical Properties

WCLL BB segment foresees EUROFER as structural material, PbLi as breeder and multiplier and water as coolant. In the present work, BB segments are assumed to be homogeneous in order to simplify the geometry: masses and volumes useful to weight the contributions are shown in table 2.1.

It's important to underline that both PbLi and water will be extracted right after the shutdown of the reactor: consequently, only 2.5% of their total amount is considered in the weighted properties calculation (it accounts for the possibility of incomplete removal). It's very likely the removed part of PbLi and water will be substituted by an inert gas, therefore, even if its weight is almost insignificant, Nitrogen is added to the calculation.

The following criteria are used to perform the calculation:

- Tungsten properties are taken as constant, values come from *WCLL Design Report* [15];

- EUROFER properties are computed with functions which are, in turn, extracted from tables of properties found inside *Material Property Handbook on EUROFER* [16];
- Water properties are computed at atmospheric pressure thanks to MATLAB XSteam tool [17];
- PbLi properties come from functions provided by *WCLL Design Report* [15]. In particular, thermal conductivity is computed with Mogahed correlation;
- Nitrogen (N_2) density is computed with ideal gas law at atmospheric pressure. $c_p = \frac{7}{2}R^*$ formulation is used to compute specific heat. Thermal conductivity is computed with a function extracted from a table found online [18].

The formulations used to obtain the weighted value of thermal conductivity and density are shown in equations 2.1 and 2.2, respectively. Specific heat is calculated with a formulation similar to equation 2.1, where specific heat substitutes thermal conductivity. V stands for volume, m stands for mass.

$$\begin{aligned} &k = \frac{a}{b} \\ &\text{where} \quad a = k_W \cdot m_W + k_{EUROFER} \cdot m_{EUROFER} \\ &\qquad +k_{H_2O} \cdot 0.025 m_{H_2O} + k_{PbLi} \cdot 0.025 m_{PbLi} \\ &\qquad +k_{N_2} \cdot \rho_{N_2} \cdot 0.975(V_{H_2O} + V_{Pbli}) \\ &\qquad b = m_{total} - 0.975(m_{Pbli} + m_{H_2O}) \\ &\qquad +\rho_{N_2} \cdot 0.975(V_{H_2O} + V_{PbLi}) \end{aligned} \tag{2.1}$$

$$\begin{aligned} &\rho = \frac{c}{V_{total}} \\ &\text{where} \quad c = \rho_W \cdot V_W + \rho_{EUROFER} \cdot V_{EUROFER} \\ &\qquad +\rho_{H_2O} \cdot 0.025 V_{H_2O} + \rho_{PbLi} \cdot 0.025 V_{PbLi} \\ &\qquad +\rho_{N_2} \cdot 0.975(V_{H_2O} + V_{Pbli}) \end{aligned} \tag{2.2}$$

All the computed values of thermal conductivity, specific heat and density are shown, respectively, in tables 2.2, 2.3 and 2.4. Due to small variation over the covered temperature range, thermal conductivity and density are assumed as constant (average value = constant). A second average is performed between Central Outboard and Left/Right Outboard segment properties to get a Outboard Sector unique value. In terms of specific heat, a fitting has been preferred to increase the simulation accuracy. Final values and expressions are shown in table 2.5.

Table 2.1: Mass and volumes estimation of WCLL BB segments [15].

			COB segment		L/ROB segment		L/RIB segment	
Material of BB components	WCLL BB Material composition	Density ($kg\,m^{-3}$)	Volume (m^3)	Mass (kg)	Volume (m^3)	Mass (kg)	Volume (m^3)	Mass (kg)
Tungsten	0.22%	$1.687{\cdot}10^4$	0.05	794.5	0.04	746.9	0.03	545.5
EUROFER	29.83%	7860	6.47	$5.087{\cdot}10^4$	6.08	$4.782{\cdot}10^4$	4.44	$2.493{\cdot}10^4$
Water	12.25%	711.4	2.66	1891	2.50	1777	1.82	1298
PbLi	57.70%	9358	12.52	$1.172{\cdot}10^5$	11.77	$1.102{\cdot}10^5$	8.60	$8.047{\cdot}10^4$
Total	100.0%		21.70	$1.707{\cdot}10^5$	20.39	$1.605{\cdot}10^5$	14.89	$1.072{\cdot}10^4$

Table 2.2: Thermal Conductivity for every material and homogenized values.

Temperature (K)	Tungsten ($W\,m^{-1}\,K^{-1}$)	Eurofer ($W\,m^{-1}\,K^{-1}$)	PbLi ($W\,m^{-1}\,K^{-1}$)	H20 ($W\,m^{-1}\,K^{-1}$)	N2 ($W\,m^{-1}\,K^{-1}$)	Homog. COB ($W\,m^{-1}\,K^{-1}$)	Homog. L/R0B ($W\,m^{-1}\,K^{-1}$)	Homog. L/RIB ($W\,m^{-1}\,K^{-1}$)
508.2	125	30.29	0.245	0.037	0.040	30.03	30.03	29.93
518.2	125	30.26	0.247	0.038	0.040	30.00	30.00	29.90
533.2	125	30.20	0.250	0.039	0.041	29.94	29.94	29.84
548.2	125	30.12	0.253	0.041	0.042	29.87	29.87	29.78
563.2	125	30.04	0.256	0.042	0.043	29.79	29.79	29.70
578.2	125	29.95	0.259	0.044	0.044	29.71	29.71	29.62
593.2	125	29.86	0.262	0.046	0.044	29.63	29.63	29.54

Table 2.3: Specific Heat for every material and homogenized values.

Temperature (K)	Tungsten ($J\,kg^{-1}\,K^{-1}$)	Eurofer ($J\,kg^{-1}\,K^{-1}$)	PbLi ($J\,kg^{-1}\,K^{-1}$)	H20 ($J\,kg^{-1}\,K^{-1}$)	N2 ($J\,kg^{-1}\,K^{-1}$)	Homog. COB ($J\,kg^{-1}\,K^{-1}$)	Homog. L/ROB ($J\,kg^{-1}\,K^{-1}$)	Homog. L/RIB ($J\,kg^{-1}\,K^{-1}$)
508.2	145	530.9	199.6	1984	1038	508.9	508.9	500.9
518.2	145	533.1	199.7	1987	1038	510.9	510.9	502.9
533.2	145	536.4	199.9	1993	1038	514.0	514.0	505.9
548.2	145	539.8	200.0	2000	1038	517.2	517.2	509.0
563.2	145	543.4	200.1	2007	1038	520.5	520.5	512.2
578.2	145	547.3	200.3	2015	1038	524.2	524.2	515.8
593.2	145	551.5	200.4	2023	1038	528.1	528.1	519.6

Table 2.4: Density for every material and homogenized values.

Temperature (K)	Tungsten ($kg\,m^{-3}$)	Eurofer ($kg\,m^{-3}$)	PbLi ($kg\,m^{-3}$)	H20 ($kg\,m^{-3}$)	N2 ($kg\,m^{-3}$)	Homog. COB ($kg\,m^{-3}$)	Homog. L/ROB ($kg\,m^{-3}$)	Homog. L/RIB ($kg\,m^{-3}$)
508.2	$1.930{\cdot}10^4$	7712	9915	0.434	0.672	2482	2475	2476
518.2	$1.930{\cdot}10^4$	7709	9903	0.425	0.659	2481	2474	2475
533.2	$1.930{\cdot}10^4$	7704	9886	0.413	0.640	2479	2473	2474
548.2	$1.930{\cdot}10^4$	7699	9868	0.402	0.623	2478	2471	2472
563.2	$1.930{\cdot}10^4$	7694	9850	0.391	0.606	2476	2470	2471
578.2	$1.930{\cdot}10^4$	7689	9832	0.381	0.591	2475	2468	2469
593.2	$1.930{\cdot}10^4$	7684	9814	0.371	0.576	2473	2467	2468

Table 2.5: WCLL weighted solid properties.

	Thermal Conductivity ($W\,m^{-1}\,K^{-1}$)	Specific Heat ($J\,kg^{-1}\,K^{-1}$)	Density ($kg\,m^{-3}$)
IB	29.86	$c_p = 3.703185 \cdot 10^{-6}T^3 - 5.716076 \cdot 10^{-3}T^2 + 3.1281943T - 1.034963 \cdot 10^2$	2472
OB	29.77	$c_p = 3.808170 \cdot 10^{-6}T^3 - 5.878952 \cdot 10^{-3}T^2 + 3.229782T - 1.139771 \cdot 10^2$	2474

2.2 Decay Heat Load

Due to the interaction with neutrons, materials inside BB experience activation. Its evaluation is fundamental because it represents an additional heat source to be cooled down with convective heat transfer. Starting point for this evaluation has been the decay heat (MW m^{-3}) found inside Tom Berry and Tim Eade report [19]. They have used the 2017 baseline DEMO WCLL 11.25° MCNP model with homogeneous blanket layers [19] to calculate decay heat value of every material inside each predefined BB layer. Summing up the contribution of every material in each layer, taking into account only 2.5% of PbLi, a unique decay heat value for the whole BB has been calculated in multiple time instant. Best-fitting of these values has been performed to obtain a time dependent decay heat function. Last step has been a time shifting: the decay heat data were calculated from shutdown onwards, whereas the present work is aimed to find a cooling time starting from 30 days after the reactor shutdown. The final decay heat expression is shown in equation 2.3 whereas the comparison between data and fit is visible in figure 2.1 (the plot shows the fitting without time scaling).

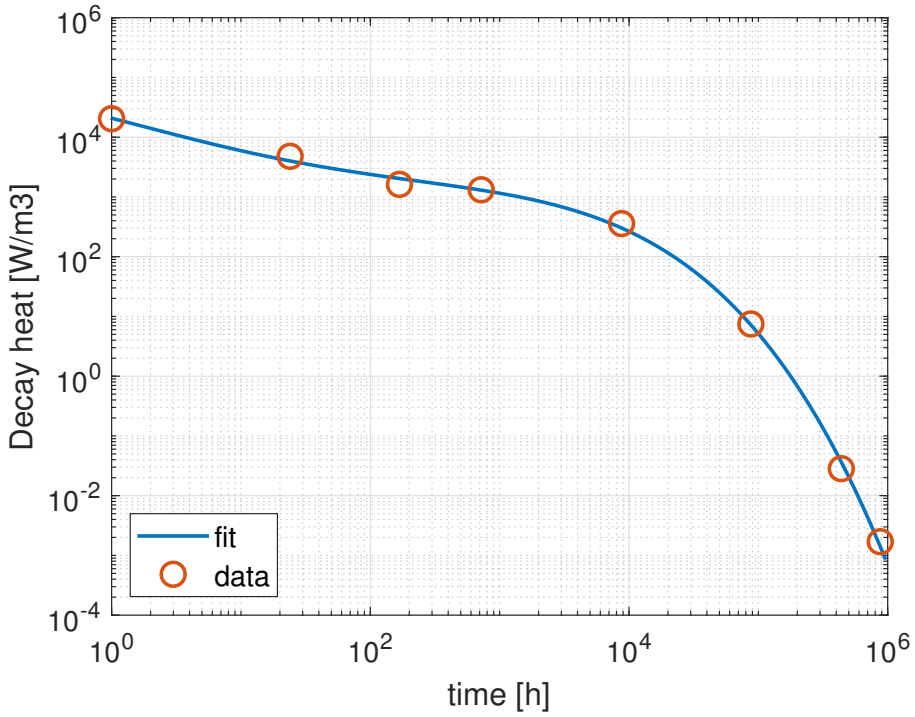

Figure 2.1: Decay heat function compared with available data.

$$q''' = exp[a\ln(t+t_0)^4 + b\ln(t+t_0)^3 + c\ln(t+t_0)^2 + d\ln(t+t_0) + e] \quad (2.3)$$

where the result is given in $\mathrm{W\,m^{-3}}$, the time must be given in s, $t_0 = 30$ days, $a = -0.001165$, $b = 0.05223$, $c = -0.8366$, $d = 5.201$, $e = 0.008689$.

It is worth mentioning that it was not possible to obtain two separate functions for IB and OB segment due to the absence of data with this subdivision, whereas it has been possible in the study performed on HCPB BB segments [14].

2.3 Natural Convection Simulation setup

The setup for WCLL BB cooled by air in natural convection is very similar to the setup used to run the same situation with HCPB BB concept [14]. Hovewer, it's worth summarizing its main features.

The reference geometry comes from the EU DEMO 2017 baseline ([20], [21]). The domain is characterized by a $\sim$ 30m long and $\sim$ 10m high toroidal chamber, inside which the cooling phenomenon occurs mostly through 2 cm thick gaps located among the segments (detailed view of a gap in figure 2.2). The air flows

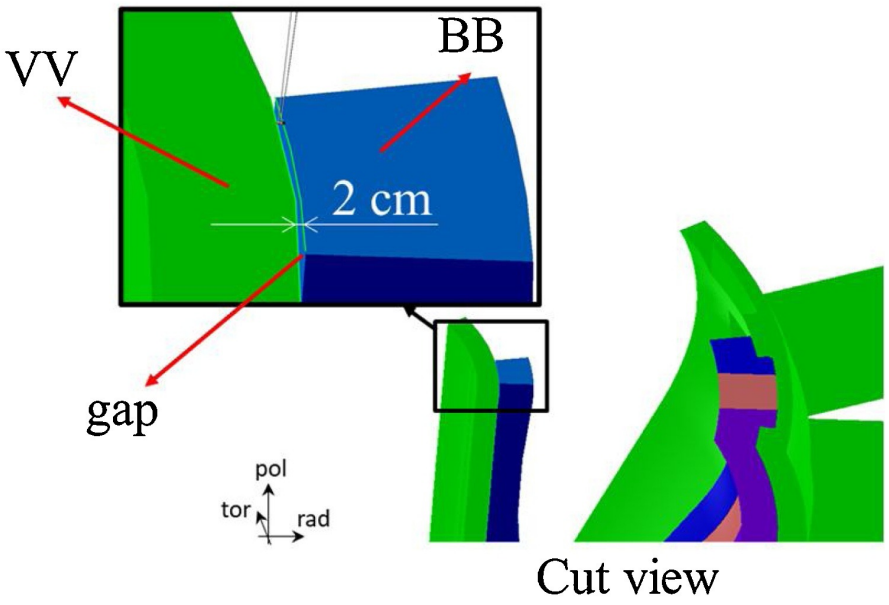

Figure 2.2: Cut view of EU DEMO sector with detailed view of the gap between BB and VV [13].

inside the vacuum vessel from the upper and the lower ports and should enters the small gaps, therefore the meshing strategy must be set to properly study these

small areas. This constraint rises significantly the mesh cell count (and in turn the computational cost). For this reason, only the maintained sector is fully modelled whereas the others are assumed to be kept constant at $\sim$ 300°C during maintenance operations. Moreover, symmetry can be exploited to halve the toroidal chamber with a vertical plane crossing in the middle the maintained sector: both BB, VV geometries and the boundary conditions are symmetric with respect to this cut. Final configuration foresees half of a WCLL BB sector and a fluid domain that covers half of the toroidal chamber.Figure 2.3 shows the computational domain together with all the boundary conditions: the upper and lower port are fluid free entrance, whereas all the other surfaces, including the equatorial port, are walls kept constant at different temperatures, the same assumed in the HCPB configuration [13].

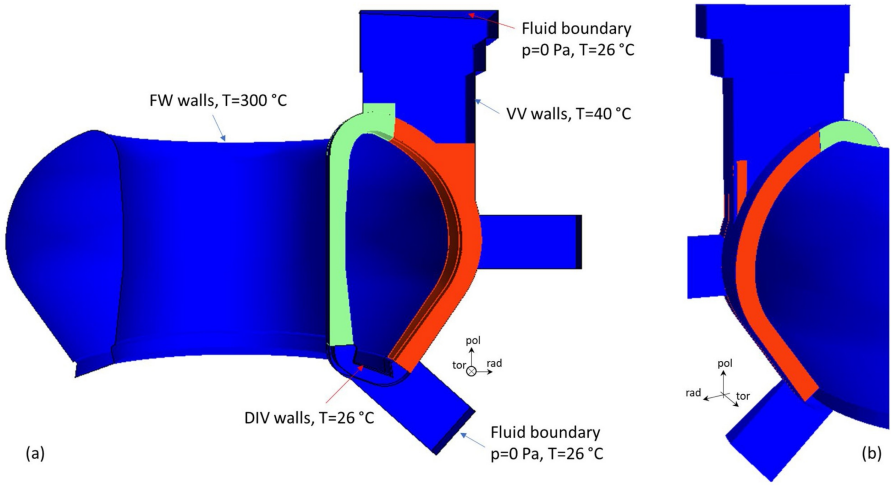

Figure 2.3: Computational domain including the boundary conditions. In green is represented the IB segment, whereas the OB is red coloured. Pressure values are Gauge ([13]).

Two different physics must be solved to fully characterise the problem: the solid one belonging to BB segments and the fluid physics defining the coolant.This configuration defines a multiscale problem wherein both advection and convection/conduction heat transfer mode plays a role. Advective time scale estimation provided in HCPB case ($\sim$ 1s, [13]) continues to be valid because chamber dimensions and parameters to evaluate stack effect relation are the same. The convection time scale is estimated as $\rho cV/(HTC \cdot A_w)$, pointing out again numerous similarities with respect to HCPB case. Indeed, solid segments volume V, wetted area A_w and heat transfer coefficient HTC are the same (the latter comes from a fully developed Nusselt number correlation in a gap-dimensioned channel and brings to $\sim 4\,\mathrm{W\,m^{-1}\,K^{-1}}$, [13]), whereas $(\rho c_p)_{WCLL}/(\rho c_p)_{HCPB} \sim 0.3$ leading to a convective

timescale estimation of $\sim 3 \cdot 10^4$.

Time Scales and *Simulation Operations* options available in STAR-CCM+ software have been used to split the two time scales and solve them with dedicated time step. The coupling between the two physics is ensured by *Simulation Operations*, which allows to switch between fluid solvers and solid solvers alternately until the overall solution converges [22]. The initial time scales setup foresees:

- Solid time equals to a constant variable (*comm_step_fluid*);
- Fluid time scale worths $\frac{1}{10}$ of the solid time scale.

This configuration allows to reduce the frequency at which the solid physics is solved, since it evolves much slower than the fluid. Moreover, it decouples the solution of solid and fluid domains, making the latter a lot faster to solve.

Meshing strategy foresees:

- *Polyhedral mesher* in both solid and fluid domain due to its capability to ensure convergence of fluid equations while reducing number of cells with respect to *tetrahedral mesher* [22];
- *Thin mesher* used to generate a prismatic type volume mesh for thin volumes within parts or regions [22]. It suits well to cover the small gaps between adjacent segments, allowing both simulation accuracy and computational cost reduction.

Figures 2.4a and 2.4b show the complete meshed domain from two different views, giving an idea of the difference in cell dimensions between the area close to the maintained sector and the rest of the chamber. A further focus on fluid domain meshing strategy is presented in the cut view of figure 2.4c. Here is visible just the lower half of the fluid domain and is clear the goodness of thin mesher, able to model with 3 layers the 2cm thick gaps even if the reference mesh cell *base size* is 0.5m. The mesh refinement in the zones close to gaps creates an important non-uniformity, because $\sim 75\%$ of the overall cell count ($\sim 4 \cdot 10^5$ cells) is located in these areas. Total cell count value is in complete agreement with HCPB case [13].

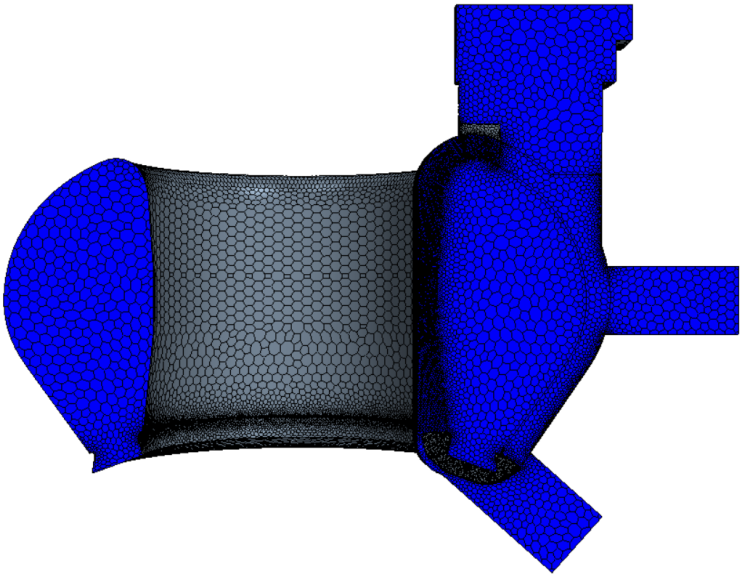

(a) Poloidal view (Symmetry plane in blue and domain walls in grey).

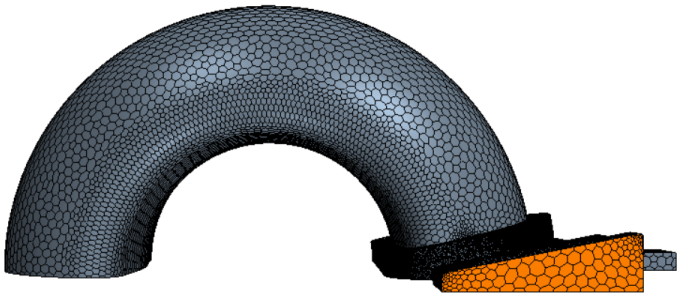

(b) Top view (Upper port air outlet in orange).

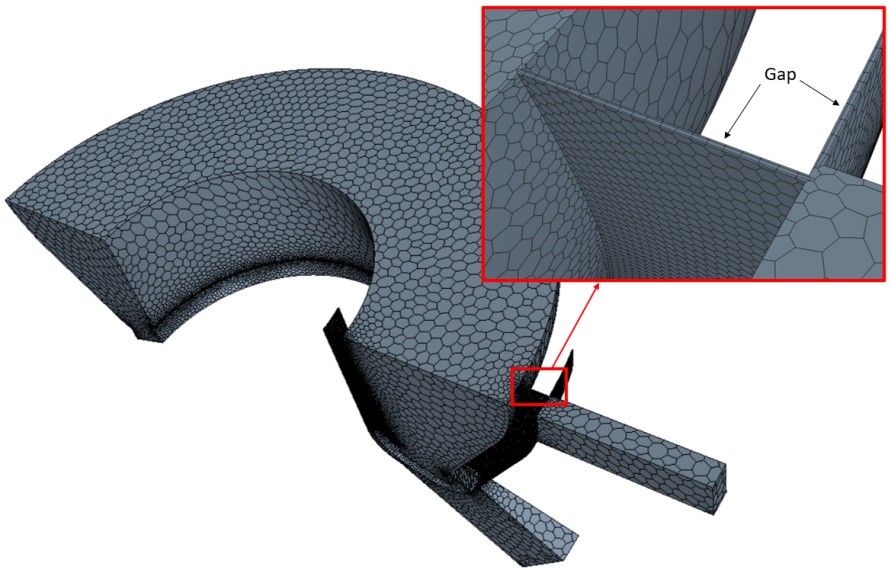

(c) Focus on fluid domain mesh with a zoom on the layers generated by thin mesher in the gap zones.

Figure 2.4: Natural convection setup mesh views.

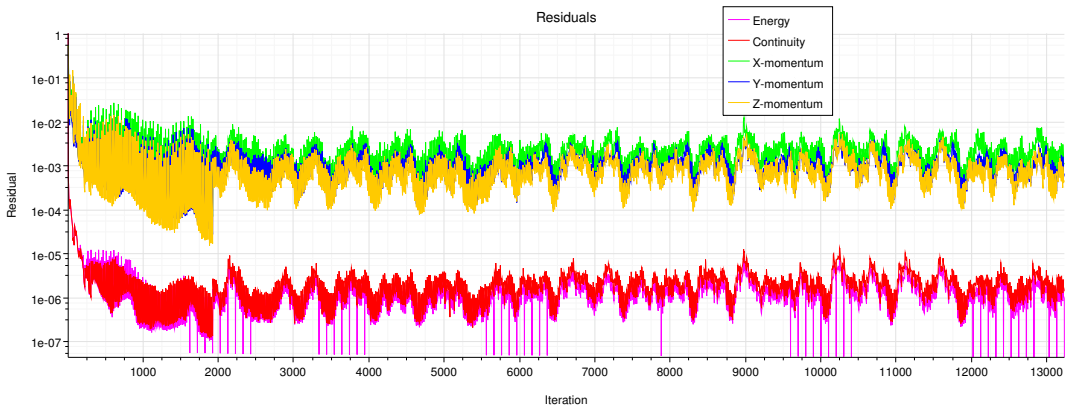

Figure 2.5: WCLL BB concept simulation residuals.

The fluid physics is solved exploiting several models, among which the most relevant are:

- Three dimensional;
- Implicit unsteady;
- Laminar;
- Constant density (air);
- Coupled flow and energy;
- Gravity;
- Boussinesq approximation.

The solid physics foresees:

- Three dimensional;
- Implicit unsteady;
- Constant density (weighted solid density).

Boussinesq approximation has been added to correctly model the natural convection while keeping the fluid density constant and solving incompressible fluid equations. Coupled approach has been preferred to segregated one because of the higher solution accuracy, even if it is counterbalanced by a slower convergence and higher computational cost. As mentioned before, the WCLL simulation is strongly

Table 2.6: Time scales adjustments to achieve convergence and simulation optimization.

Step (-)	*comm_step_fluid* (s)	*First Iteration* (-)	*Last Iteration* (-)
1	1	1	1900
2	5	1901	5900
3	8	5901	13000

similar to HCPB setup [14] becuase it has been changed only the solid weighted properties and the heat load function.

As normally occurs in CFD simulations, first iterations are the most difficult to reach convergence and shorter time steps are necessary to avoid issues. On the other hand, once exceeded this critical part, the time step should be increased to reduce the simulation computational cost. Here *comm_step_fluid* has been increased after convergence achievement, optimizing the subsequent iterations. Table 2.6 shows the initial taken steps. Figure 2.5 shows the simulation residuals behaviour in the first part of the simulation (from the beginning until $\sim$ 13000 iterations). The effectiveness of solution strategy is testified by their decrease up to $10^{-2} - 10^{-3}$ values, kept even when the *comm_step_fluid* has been increased.

2.3.1 Independence study on *comm_step_fluid*

The third step shown in table 2.6 has been repeated with other *comm_step_fluid* values. This procedure aims to calculate error of solutions solved with higher *comm_step_fluid* with respect to a selected benchmark, going towards further computational cost reduction. Indeed, since the order of magnitude of the simulated transient is (at least) tens of days, High Performance Computing (HPC) facility becomes necessary to solve the problem in a reasonable time. Once using HPC, it is even more important to keep as low as possible the computational effort; It is common procedure to solve individually the first part of the transient in order to implement the right setup and verify the residuals convergence. Once the goodness of the simulation is assessed, it is brought to HPC to complete the solution. Simulation solved with *comm_step_fluid*$= 5s$ is the selected benchmark of the present study. It is compared with simulations performed with *comm_step_fluid*$= 8s, 10s, 15s, 20s$. Important physical quantities are used to make the comparison: Average temperature in the fluid, average temperature and maximum temperature in the solid domain.

$$\text{Error} = \frac{|T_{benchmark} - T|}{T_{benchmark}} \cdot 100 \quad (\%) \tag{2.4}$$

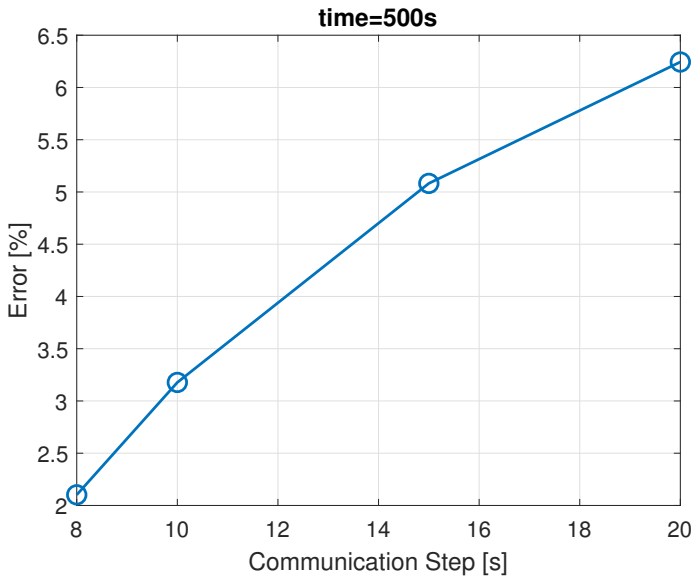

Figure 2.6: Fluid average temperature relative error calculated in a precise time instant (500 seconds).

Figures 2.6 and 2.7 show the results. Error is always computed as shown in equation 2.4. As expected, in both cases the error increases when the *comm_step_fluid* increases. Error on fluid temperature shows the highest values, even if it never overcomes 6.5%. Errors on solid temperature are almost negligible in all the selected setup. Since solid temperature increases when accuracy decreases, the simulation with higher time steps goes in safe direction: the cooling time will never be underestimated. In view of these considerations, the highest *comm_step_fluid* has been selected to continue the transient resolution exploiting HPC.

2.3.2 Independence study on fluid time scale

A second investigation has been performed on the coupling between fluid and solid time scales. Here *comm_step_fluid* has been left constant (equal to 8s) whereas it has been varied the multiplicative coefficient shown in equation 2.5. The aim is similiar to the prevoius independence study: see to reduce the simulation computational cost rising the fluid time scale, the most delicate one.

$$\text{fluid time scale} = C \cdot \textit{comm\_step\_fluid} \tag{2.5}$$

Simulations have been performed with $C = 0.1, 0.2, 0.4, 0.8$. $C = 0.1$ has been selected as benchmark in the errors evaluation. Figures 2.8 and 2.9 show the results. Similarly to the previous calculations, errors on solid average temperature

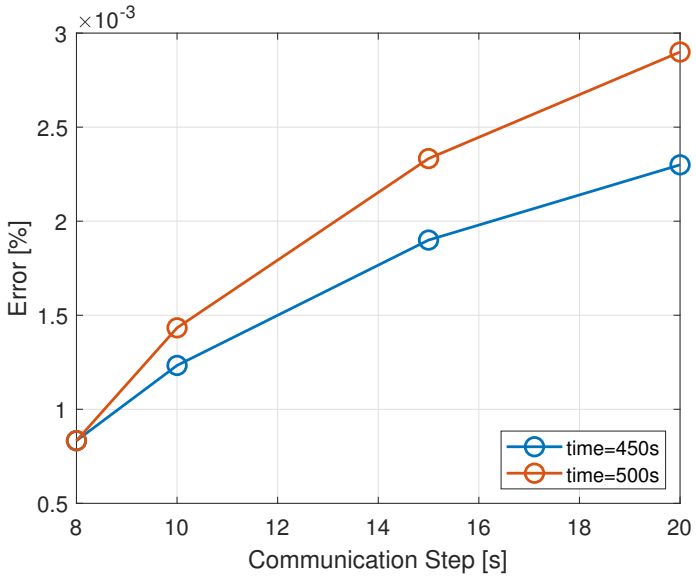

(a) Relative error

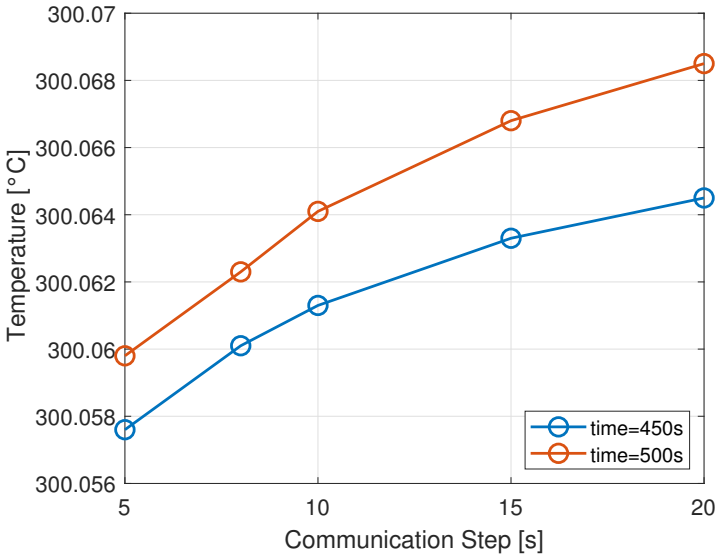

(b) Solid average temperature

Figure 2.7: Solid temperature magnitude and relative error calculated in two time instants.

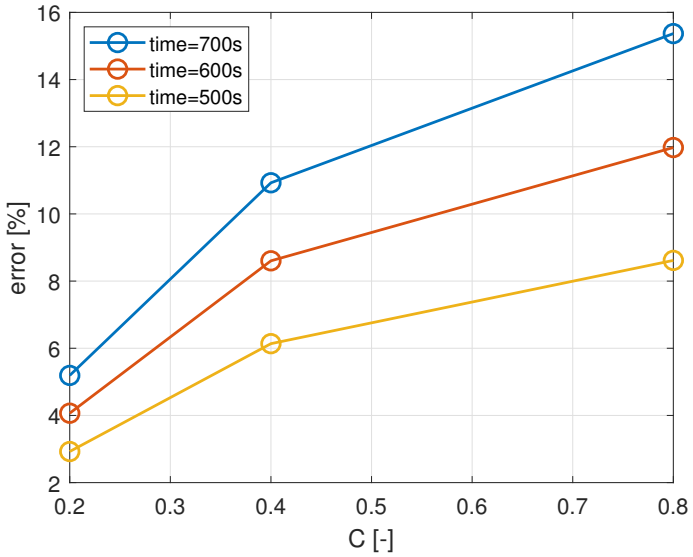

Figure 2.8: Fluid average temperature relative error with respect to solution with $C = 0.1$ calculated at 3 time instants.

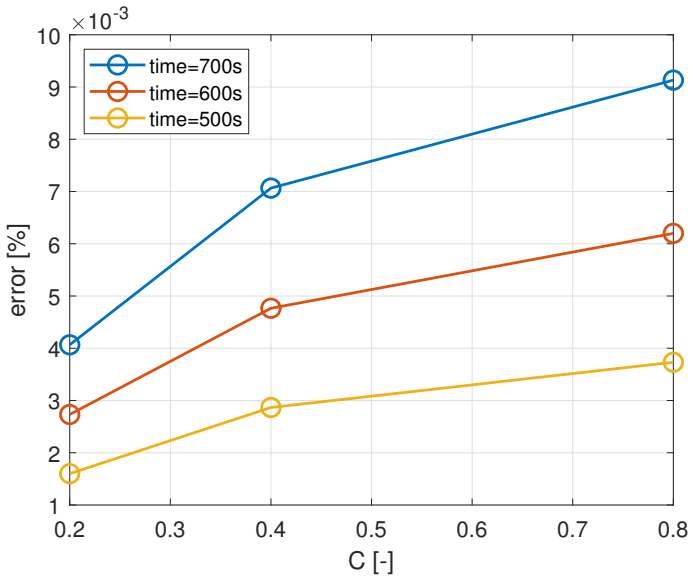

Figure 2.9: Solid average temperature relative error with respect to solution with $C = 0.1$ calculated at 3 time instants.

are always really small. On the other hand, errors on fluid temperatures rise with the simulation time and the value of C, going up to $\sim 15\%$. $C = 0.2$ (the value adopted in the 3D simulations) represents a good compromise between computational cost (it would be halved with respect to the benchmark) and accuracy, with calculated errors always lower than $\sim 6\%$. However, $C = 0.1$ is a reasonable choice as well: since the fluid temperature error rises with the simulation time, it could reach non negligible magnitude even in case of $C = 0.2$. The other two cases provide too large errors (considering the limited simulated time from which they rise) to be selected.

2.3.3 Results

A 0D analysis performed with ordinary differential equation (ODE) shown in equation 2.6 gives a rough estimation of $\sim$ 190days to cool down the BB segments (see figure 2.10).

$$\rho c_p V \frac{dT}{dt} = q''' V + HTC \cdot A_w (T_f - T) \tag{2.6}$$

In equation 2.6, ρ and c_p are the averaged thermophysical properties, V, A_w and HTC are respectively volume, wetted area and heat transfer coefficient as described above in the time scales estimation (values taken from [13]), q''' is the instantaneous decay heat, T_f is the fluid temperature, taken as constant and equal to 26 °C. It is important to highlight that this estimate is non-conservative, since it gives an average temperature of the solid whereas the important quantity is the maximum segment temperature and the presence of warm adjacent segments is neglected. Even if the WCLL thermal capacity value is about three times lower than the HCPB, the difference in decay heat leads to a cooling time estimation about 9 times higher. Indeed, as shown in figure 2.11, the ratio between WCLL and HCPB decay heat rises monotonically and, starting from $\sim$ 1.3 after 1 day, reaches $\sim$ 5 after 38 days and $\sim$ 9 after 109 days. Moreover, in figure 2.11 are plotted decay heats from reactor shutdown onward, whereas IVCs cooling is calculated starting from 30 days after shutdown. Therefore, at the beginning of IVCs cooling simulation, the WCLL decay heat is already $\sim$ 5 times higher than HCPB.

Figures 2.12 and 2.13 report respectively the evolution of maximum and average solids and air temperature. The simulated transient is also compared with the 0D rough estimation. At present, just the solid part of the lines represents a simulated value, whereas dashed lines are extrapolated values from the exponential behaviour already simulated. Indeed, as shown by results, the time to completely cool down from 300°C to 150°C IB and OB segment of the maintained sector is, respectively, $\sim$ 352 and $\sim$ 228 days.

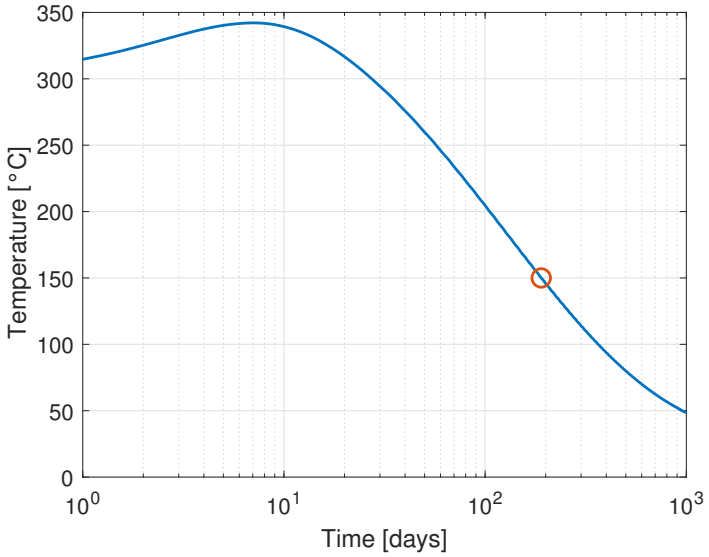

Figure 2.10: Time evolution of averaged BB segments temperature in 0D (lumped) model analysis.

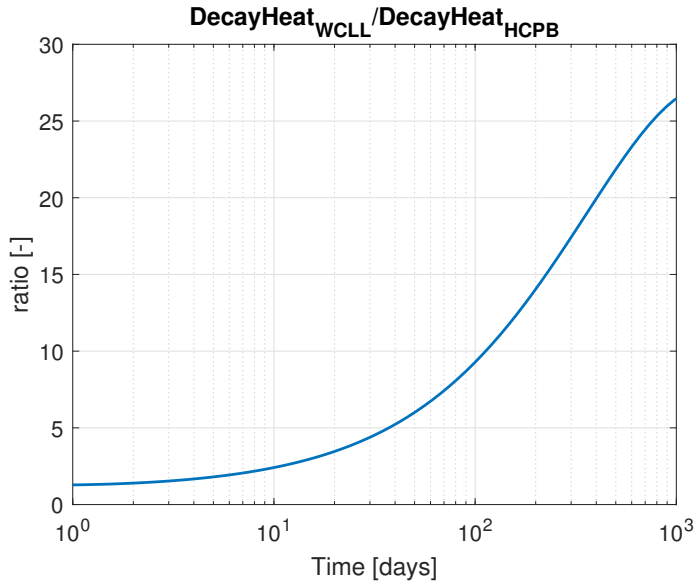

Figure 2.11: Time evolution of decay heat ratio between the two BB concept.

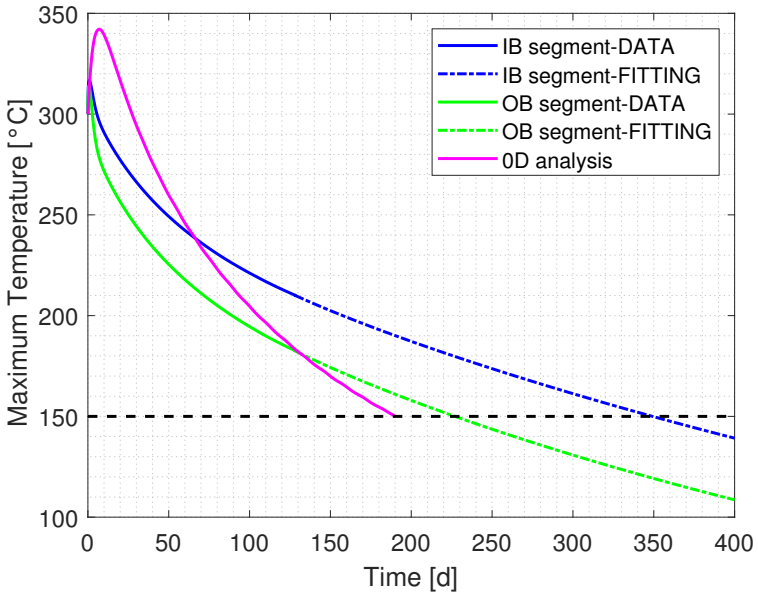

(a)

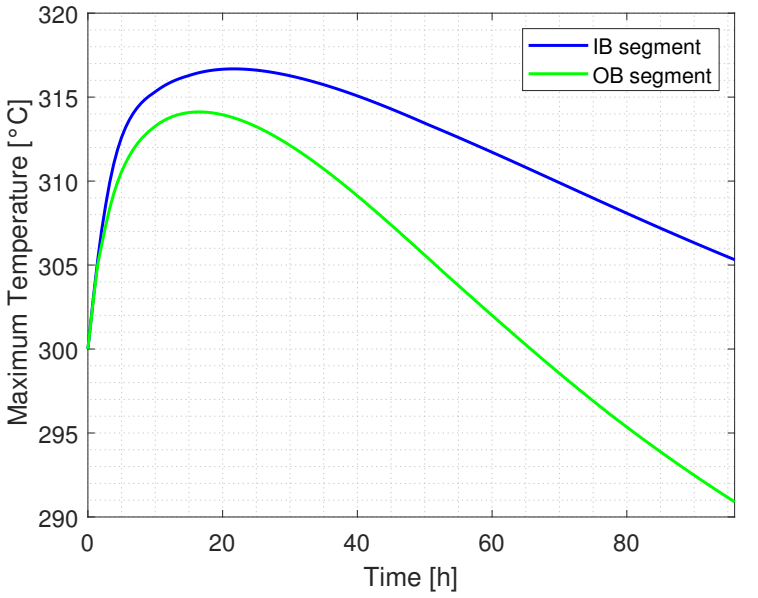

(b)

Figure 2.12: Solid segments and fluid domain maximum temperature evolution in time. Figure (a) shows the overall evolution compared with the 0D analysis. Solid lines are simulated values, dashed lines are extrapolated values. Horizontal dashed line is the 150°C threshold. Figure (b) gives a focus on the first hours of simulation, where solid segments maximum temperature rises because of decay heat. Note that both temperature and time scales are different in the two plots.

These extremely high transient duration leads to equally high simulation time, not completed yet. However, the above mentioned value extrapolation already gives a good estimate of the transient time, which seems to be too long to be applied in a real configuration (the overall colling time is already ∼5 months). Moreover, it must be taken into account that this estimate is non-conservative: it does not consider that the heat transfer effectiveness will decrease as the temperature difference between solid and cooling medium will decrease, leading to longer time to reach 150°C. As expected, also the 0D analysis results to be non-conservative, even if it foresees a higher overall transient maximum temperature. In figure 2.12b is clearly visible the decay heat contribution, which predominates the cooling for ∼ 22 hours and brings the IB segment maximum temperature up to ∼ 316°C. The initial heating is larger with respect to HCPB (see [13]), both in strength and duration, as justified by figure 2.11, but it is again negligible compared to the transient total length.

Figure 2.13 shows the behaviour of average temperatures, calculated as volume average over all the sector domain (the solid average) and all the fluid domain. Again an extrapolation (dashed lines) indicates the tendency of the solid to reach the mean air temperature (∼ 95°C). Notice that, as mention before, the extrapolation does not reflect completely the reality: here it seems the solid mean temperature will become lower than the fluid one, but this is not possible. The extrapolation does not take into account the physics behind heat transfer, the heat source will always be slightly hotter than the coolant.

Figure 2.14 shows in detail the motion field. Velocity magnitude inside the chamber reaches the highest values at the segments bottom, close to the divertor (especially visible the area near IB segment), at the border between segments and the upper port and in all the segments gaps (partly visible in bottom OB segment detail of figure 2.14). The air flows mainly vertically from the lower port towards the upper one, thanks to stack effect. Indeed, as visible from the upper port detail of figure 2.14, the flow through the upper port is mostly outwards. This flow is in complete agreement with natural convection principles and HCPB similar simulation (see [13]).

From figure 2.12a is clear the difference in cooling time between IB and OB segments (see also temperature field below in the discussion). However, figure 2.15, that compares the velocity field at IB and OB gap, reports quite similar motion field and, in turn, similar heat transfer parameters. Moreover, as testified by figure 2.14, the lower port shape and configuration makes easier the flow towards IB segment. The concerned difference should then rise from the geometry of the machine. OB segment rear and side gaps have direct connection with the upper port (warm air is easily take away), whereas part of the warm air from IB gaps could be stuck in the top part of the chamber, leading to difficulties in the warm

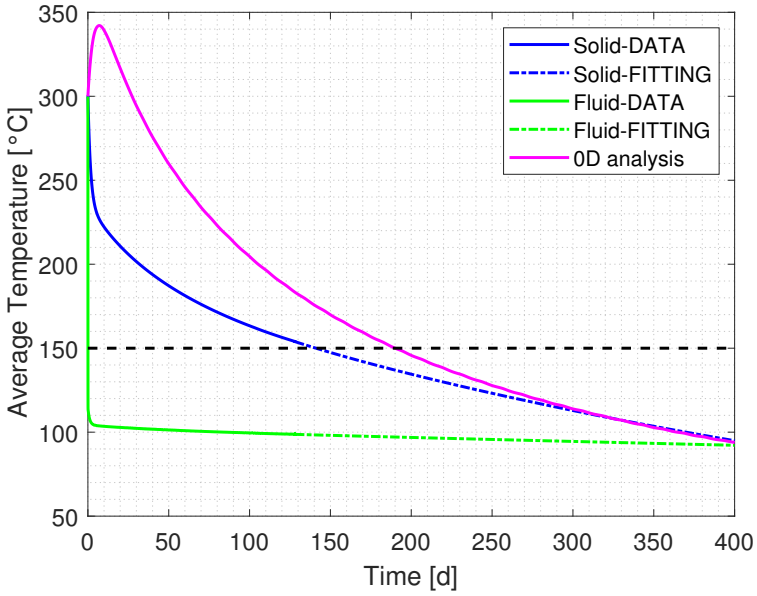

Figure 2.13: Solid segments and fluid domain average temperature evolution compared with 0D analysis. Solid lines are simulated values, dashed lines are extrapolated values.

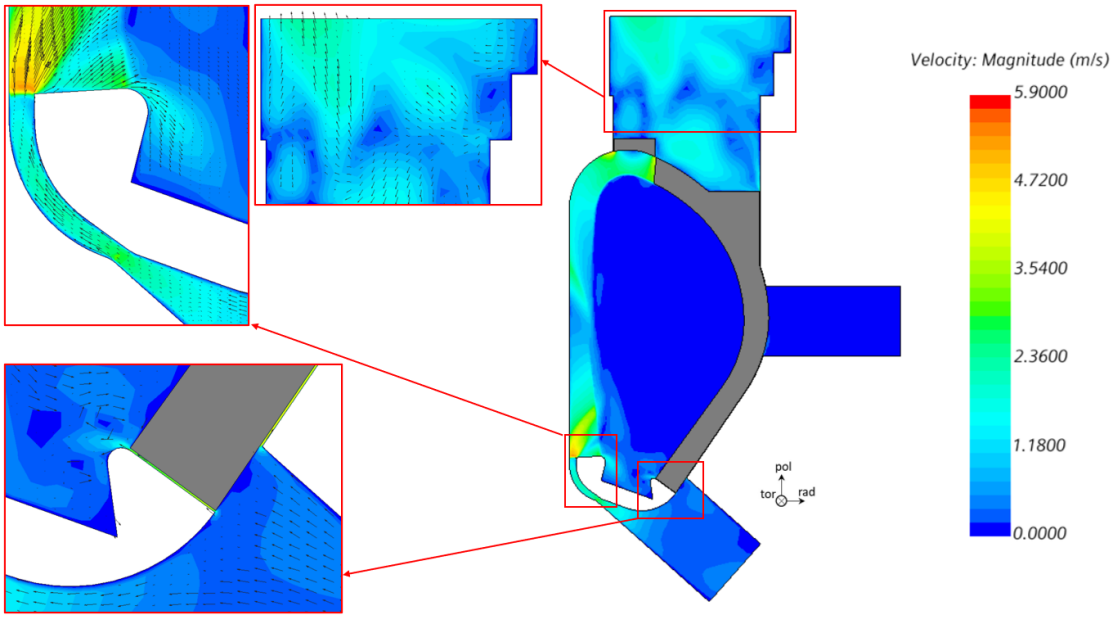

Figure 2.14: Velocity field magnitude at symmetry plane, 6 days and 12 hours after the transient beginning. The three red bordered details show also the vectorial field at segments bottom and at the upper port of the vacuum vessel.

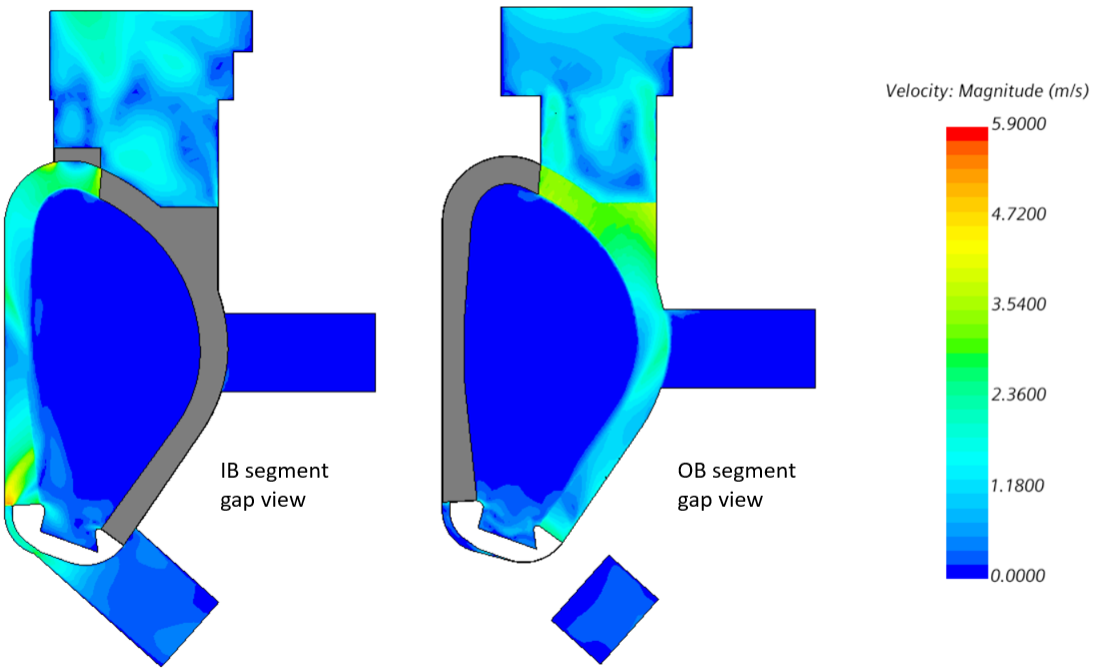

Figure 2.15: Velocity field magnitude at IB and OB segment gaps.

air removal. In any case, in order to speed up the process, RH procedure could start from OB segment while the IB is still cooling down.

Figure 2.16 describes symmetry plane temperature distribution taken at different time instants. As consequence of the upwards air motion described above, the BB segments start to be cooled down from the bottom part, whereas the RH equipment will probably grab them from the top. Since the RH equipment attach position cannot be modified, the natural convection does not represent the best approach to optimize the cooling procedure. Exponential behaviour of heat transfer process is again pointed out: most of the OB segment is cooled down from $\sim$ 310°C to at least $\sim$ 240°C in the first 6.5 days of transient, than it takes 30 days bring the segment upper half from $\sim$ 220°C (at time=28 days) to $\sim$ 210°C (at time=58 days). In contrast with HCPB (see [13]), here the cooling process continues to be unfeasible even if the operation window of RH systems would be enlarged: the cooling period to reach 170°C is $\sim$ 163 days for OB segment and $\sim$ 267 days for OB segment. Taking into account there are 16 sectors that sooner or later should be maintained, it could be difficult to finish the maintenance of all the sectors before the first maintained one has to be removed again. Forced convection could be a solution to keep the WCLL an attractive BB option.

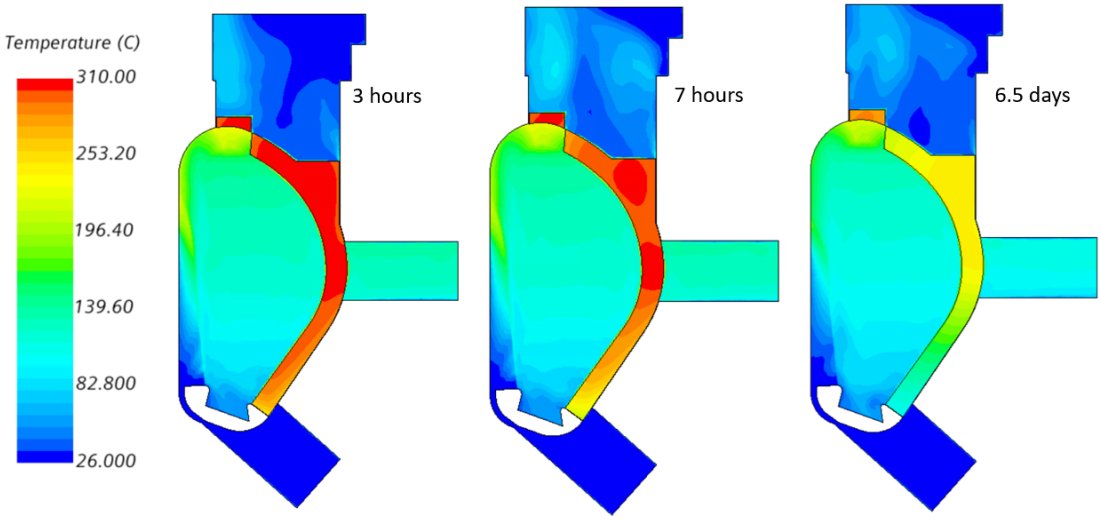

(a)

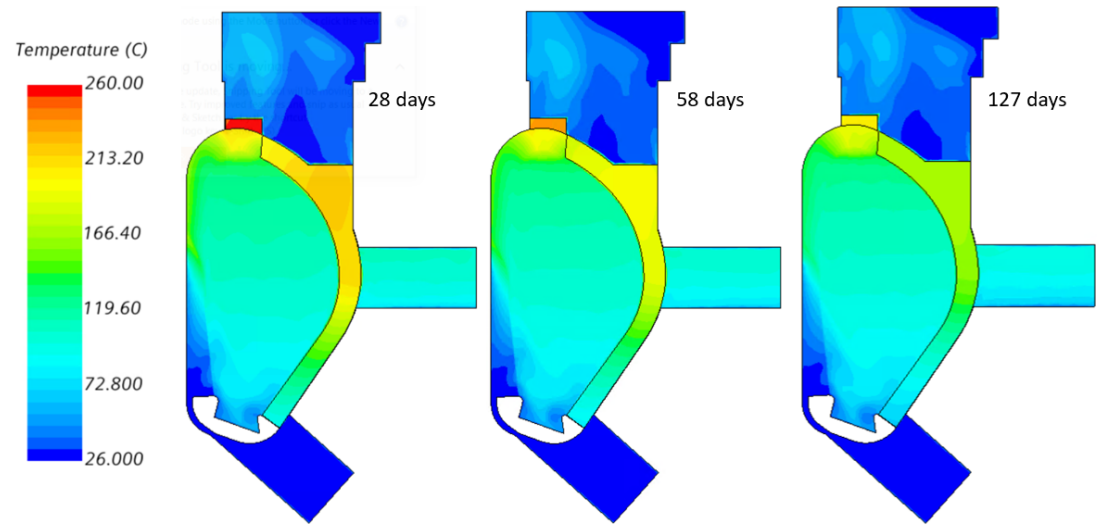

(b)

Figure 2.16: Temperature field on symmetry plane at different instants. Two temperature scales are used in (a) and (b) to better visualized the temperature distribution.

Chapter 3

Turbulent Simulations

Natural Convection setup has been useful to get an estimation of the cooling duration in case of a passive strategy and it has been the first case to be investigated because of the lower simulation complexity. However, investigation results point out that, almost certainly, it is not a viable solution. Forced convection of air inside the plasma chamber is a possible option to increase the cooling effectiveness, using a fan or a similar machine. In this framework, the imposed air mass flow rate will certainly create instabilities inside the flow, causing turbulence to play a key role in the problem. Moreover, due to the geometry of the volume cooled by air, which shows abrupt cross area changes, it is very likely the flow won't be laminar.

Turbulent flow means highly unsteady flow, in which all the physical quantities under investigation are subject to random and chaotic changes. It is characterize by a high degree of three-dimensional vorticity, causing mixing among fluid parcels with different momentum content. In this framework, Navier-Stokes equation solution becomes more difficult and some of the approximation used to describe laminar flow are no longer valid. One of the most significant example is the shear stress (τ): it is simply proportional to the velocity gradient in a laminar pipe flow, whereas in turbulent it contains also shear force contribution coming from velocity random changes. Equation 3.1 shows the two definition for two-dimensional flow. μ stands for dynamic viscosity, $\overline{u}$ is the velocity vector, $-\rho\overline{u'v'}$ is the turbulent contribution.

$$\tau_{laminar} = \mu\frac{\partial\overline{u}}{\partial y} \qquad\qquad \tau_{turbulent} = \mu\frac{\partial\overline{u}}{\partial y} - \rho\overline{u'v'} \tag{3.1}$$

The most accurate approach to turbulence simulation is the so-called direct numerical simulation (DNS). As suggested by the name, it solves directly (without approximations) the Navier-Stokes equations, therefore all the flow irregularities are properly characterized. This solution strategy is extremely expensive in terms

of computational cost, since it requires both really fine grid size (to catch the three dimensional flow fluctuations) and short time scale. For this reason, this method is used just for simple geometry and low-Reynolds number flows and it is considered mainly as a research tool [23]. Another solution approach, far more useful from the engineering point of view, splits turbulent flow quantities in terms of their mean value together with a fluctuating component. The mean value comes from a time average over a sufficiently long time interval, large with respect to fluctuations time scale. Applying this process to Navier-Stokes equation lead to the so-called Reynolds-averaged Navier-Stokes (RANS) equation. Equation 3.2 shows the x-component of the set of RANS, where U is the mean component of the velocity, $\overline{u}$ is the fluctuating one. Vectorial quantities are bolded.

$$\frac{\partial U}{\partial t} + div(U\mathbf{U}) + div(\overline{u'\mathbf{u}'}) = -\frac{1}{\rho}\frac{\partial P}{\partial x} + \nu div(grad(U)) \tag{3.2}$$

The third term of equation 3.2 is the new one with respect to classic Navier-Stokes and it can be further decomposed in three contribution, among which the *Reynolds stresses* (second term in turbulent shear stress equation written in eq.3.1). The presence of these new variables makes the set of equation under-determined (number of variables higher than number of equations). Closure equations are required to complete the model and some approximations are normally used to get the closure. According to the number of closure equations, one can distinguish among different RANS turbulence models. As the number of equations increase, the adopted approximation degree should be lower, but always present in some extent. RANS approach is one of the most adopted among CFD computation because it provides a good compromise between computational cost and accuracy (in most of the engineering problem, it is enough to know mean flow properties rather than specific turbulence characteristics). Turbulence model chosen for the present work belongs to RANS as well.

Due to the complexity of the real 3D problem, it is extremely difficult to know a priori which are the best models to set up in the CFD simulation. It is common practise to start from simplified cases in order to compare the obtained results with correlations found in literature (normally available only for simple geometry). Once assessed the agreement between simulation and correlations, it is reasonable to think the modelling setup and the selected mesh could be effective even in more complex situations. The following sections will present the simplified problems chosen to approach the complex problem and the final complete setup.

3.1 2D gap model

First simplified case is the model of a narrow horizontal rectangular duct. The real 3D problem foresees the equatorial port of the BB segment as inlet for the air in forced convection. The biggest air velocity gradients are expected to be where the equatorial port section turns into the narrow gap between two adjacent BB segment sections. It becomes necessary to investigate the heat transfer behaviour in the gap zone, due to its proximity with this critical area and its complexity in terms of meshing strategy. Starting from 3D gap configuration, the domain has been simplified in 2D because, due to symmetry, the flow is fully characterized regardless the height of the gap. Figure 3.1 shows the 2D gap domain, which, exploiting the symmetry, has been further halved in the flow direction to reduce the simulation computational cost. Even if the real length of gaps in the reactor should be in the order of 1 meter, here the length has been doubled to ensure fully developed flow in hydraulic and thermal sense. Duct hydraulic diameter is worth twice the gap width thanks to an reasonable approximation (gap width (W) value is negligible with respect to gap height (H), see equation 3.3).

$$D_h = \frac{4 \cdot (CrossArea)}{Perimeter} = \frac{4(W \cdot H)}{2(W + H)} \simeq \frac{4(W \cdot H)}{2H} = 2W \tag{3.3}$$

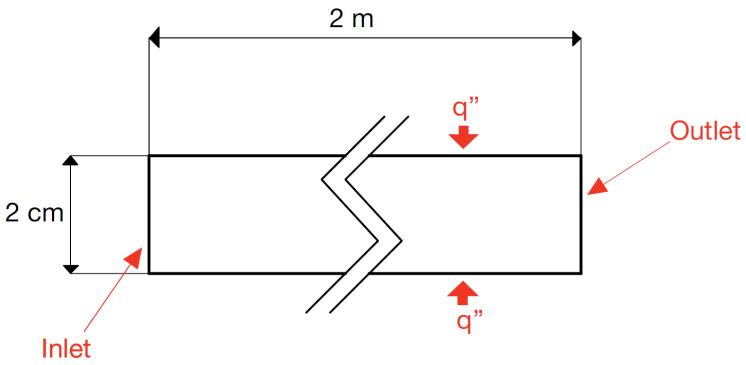

Figure 3.1: Sketch of the domain considered in the first validation case.

The simulation applied boundary conditions are:

- *Velocity Inlet*: constant velocity deduced from prescibed mass flowrates values (in the range of $0.1 - 0.5\ \mathrm{kg\,s^{-1}}$);
- *Pressure Outlet*: 0 Pa as gauge pressure;
- *Symmetry Plane*: used for the centerline of the gap;

- *Heated Wall*: to take into account the heating coming from BB segment. It has been set constant and uniform at $100\,\mathrm{W\,m^{-2}}$.

External environment conditions are 0 Pa (gauge pressure) and 300 K.

Concerning meshing strategy, *Polygonal mesher* has been coupled with *Prism layer mesher* in view of the expected turbulence. Indeed, *Polygonal mesher* builds meshes easily and efficiently and it is the two-dimensional version of *Polyhedral mesher*, the reference solution to get complex 3D meshes [22]. *Prism layer mesher* generates orthogonal prismatic cells next to the wall surfaces, able to better characterize the near wall flow behaviour. This is necessary when solving turbulent problems, where velocity and temperature gradients normal to the wall are really steep. According to the selected turbulence model wall treatment, near wall viscous sublayer can be solved directly or predicted through a wall function [22]. Figure 3.2 shows an example of adopted grid.

Calculated Re numbers always exceed 10^4, confirming the presence of turbulence. The dimensionless group Gr/Re^2 (see equation 3.4 for Grashof number

$$Gr = \frac{g\beta(T_s - T_\infty)D_h^3}{\nu^2} \tag{3.4}$$

formulation, where g is the gravity acceleration, T_s is the solid surface temperature, T_∞ is the core fluid temperature, ν is the kinematic viscosity of the fluid and $\beta = \frac{1}{T_\infty}$ for ideal gas), used to assess the presence of mixed convection [24], is always way lower than one, meaning forced convection strongly prevalent over natural convection. Consequently, it is not necessary to take the latter into account.

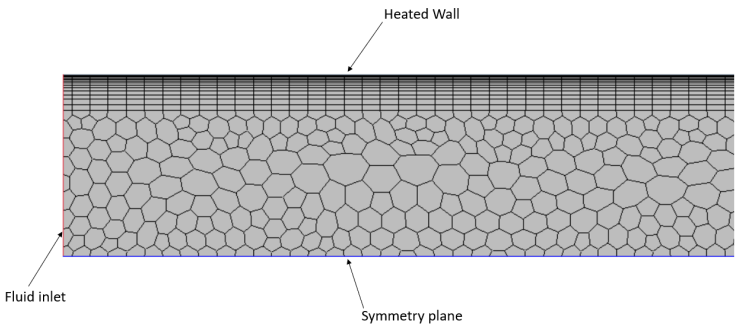

Figure 3.2: Qualitative view of the mesh adopted in 2D gap model, with Prism Layers (top part, close to the gap boundary) and Core mesh (middle and bottom portion).

Simulation has been set up in two dimensional and steady state with constant properties (air properties). Segregated flow solver has been selected because normally preferred to Coupled flow solver in case of incompressible flow, provided

that gravity is not present [22]. Moreover, Segregated flow solver allows faster solution convergence. Segregated Fluid Temperature is activated as Segregated fluid energy model. K-Omega SST is the selected RANS turbulence model. It is the recommended model for most applications, due to the exploitations of k-Epsilon model characteristics in the region far from the wall with some improvements in the near-wall region [22]. K-Omega SST has been selected with an all-y^+ wall treatment. When available, this is always the recommended choice because it is able to decide on the viscous sublayer resolution mode according to the available mesh refinement [22].

Validation of applied models and meshing strategy is performed comparing Nu number with correlations available in literature. Concerning simulations, Nu has been calculated at the domain outlet, at $x = 2m$. Indeed, even if figure 3.3 shows an hydraulically fully developed flow far before the outlet, the flow thermal development has been achieved just close to the domain edge. A localized evaluation at domain outlet instead of an average over multiple locations has been preferred for this reason. Fully developed Nu number correlations have been used

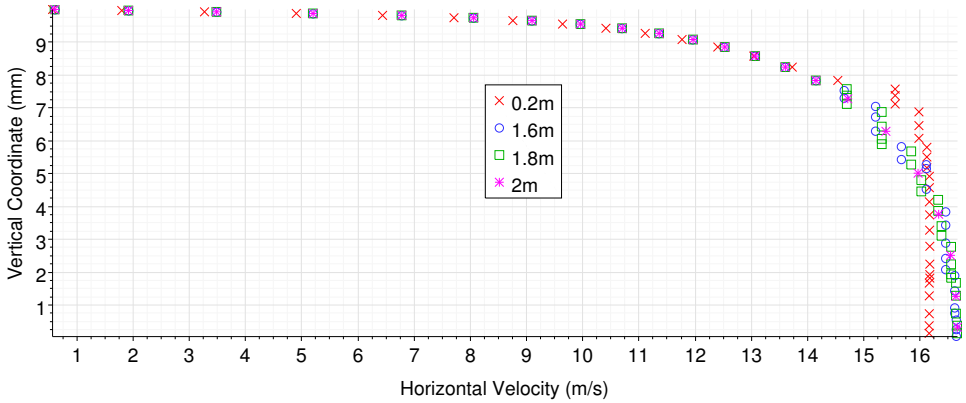

Figure 3.3: Velocity profile evaluated on planes perpendicular to the flow direction, located as shown in legend.

to make comparisons: *Dittus-Boelter* shown in equation 3.5 [24], *Gnielinski* shown in 3.6 [24] and another type of *Gnielinski*, without friction factor, shown in equation 3.7 [25]. Darcy friction factor (f_D) in the first *Gnielinski* correlation has been evaluated with *Colebrook* implicit formulation shown in equation 3.8 [24].

$$Nu = 0.023 Re_{Dh}^{4/5} Pr^{0.4} \tag{3.5}$$

$$Nu = \frac{(f_D/8)(Re - 1000)Pr}{1 + 12.7(f_D/8)^{0.5}(Pr^{2/3} - 1)} \tag{3.6}$$

$$Nu = 0.0214(Re^{0.8} - 100)Pr^{0.4} \tag{3.7}$$

$$\frac{1}{\sqrt{f_D}} = -2.0log\left[\frac{e/D}{3.7} + \frac{2.51}{Re_{Dh}\sqrt{f_D}}\right] \tag{3.8}$$

Figure 3.4 shows the results, taking into account 20% error in *Dittus-Boelter* computations and 15% error in *Gnielinski* computations. The plot shows an increasing deviations between correlations and simulation as Re increases. However, it is reasonable thinking in the real problem the air flow will usually have Re number in the simulated range, therefore the agreement with correlation at higher Re should have a lower degree of importance in the overall problem.

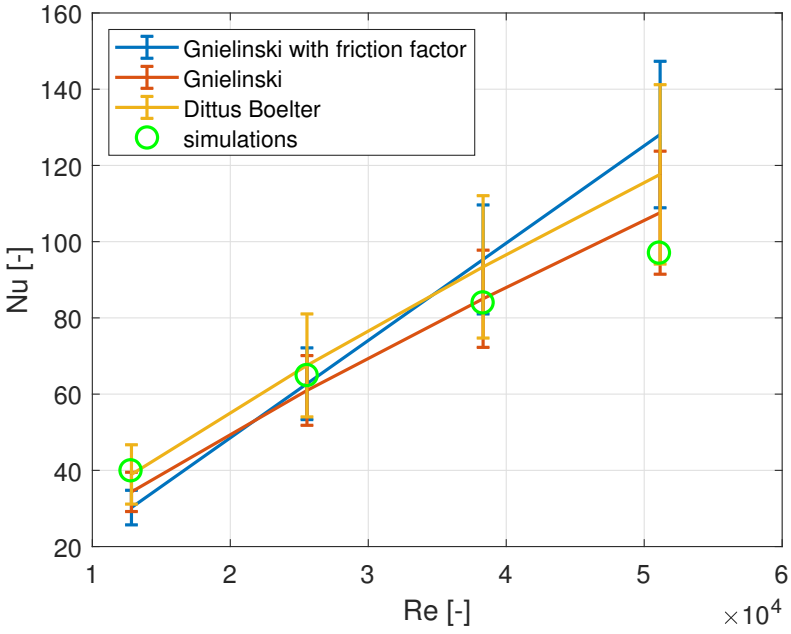

Figure 3.4: Nu calculated with correlations and values from simulation, computed at different Re.

Grid independence study has been carried out to ensure mesh reliability. Richardson extrapolation has been used to find an estimation of exact quantities starting from values obtained with three different grids [26].The average grid spacing (h) calculation, starting point of the overall analysis, has been evaluated for every mesh with equation 3.9, taking 1 m as domain height to define the domain volume. Grid spacing values are listed in table 3.1. Second step defines the *grid refinement ratios*, as shown in equation 3.10. Equations 3.11 and 3.12 are useful to evaluate the so-called *accuracy order* - p and, finally, the extrapolated value is found thanks to equation 3.13. f stands for the investigated quantity and every subscript defines a grid, according to the numbers assigned in table 3.1, in which

are listed the 3 investigated cases. Relative error with respect to the extrapolated solution has been calculated as mentioned in equation 3.14.

Figure 3.5 shows the grid independence results. Nusselt number calculated at domain outlet have been used to compute the errors at different Reynolds number. Meshing goodness is testified by the extent of the discretization errors, which is always under 1%. If other investigations had been necessary, even the coarsest grid would have been sufficient to get reliable results.

$$h_n = \sqrt[3]{\frac{(\text{Volume})_n}{(\text{Number of cells})_n}} \quad (m) \tag{3.9}$$

$$r_{21} = \frac{h_2}{h_1} \quad r_{32} = \frac{h_3}{h_2} \tag{3.10}$$

$$p = \frac{\left| \ln\left|\frac{f_3 - f_2}{f_2 - f_1}\right| + \ln\left(\frac{r_{21}^p - s}{r_{32}^p - s}\right) \right|}{\ln(r_{21})} \tag{3.11}$$

$$s = \text{sign}\left(\frac{f_3 - f_2}{f_2 - f_1}\right) \tag{3.12}$$

$$f_{exact} \simeq f_1 + \frac{f_1 - f_2}{r^p - 1} \tag{3.13}$$

$$\text{Error} = \frac{|Nu_{exact} - Nu|}{Nu_{exact}} \cdot 100 \quad (\%) \tag{3.14}$$

Table 3.1: Selected meshes main features.

Mesh number	Number of cells (-)	Base size (mm)	Surface growth rate (-)	Number of prism layers (-)	Prism layer near wall thickness (mm)	Grid spacing (m)
1	45416	1	1.2	15	0.03	0.0096
2	36269	1.2	1.3	15	0.03	0.0103
3	28877	1.4	1.3	14	0.03	0.0111

3.2 Equatorial port 2D model

Second test case includes the gap modelled in section 3.1 together with the VV equatorial port. According to 2017 EU DEMO design geometry [20] [21], the equatorial port will be around 4500 mm long, 1600 mm wide and 2800 mm high and it is foreseen to be the cooling air inlet, whereas top and bottom ports will be

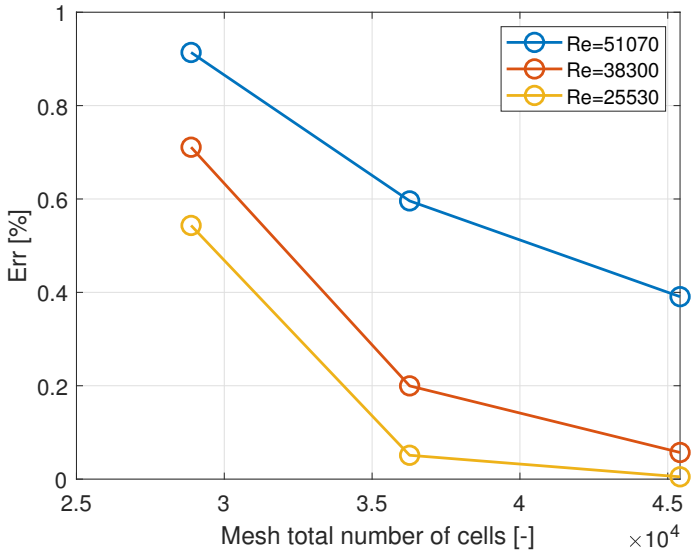

Figure 3.5: Nu number relative error with respect to extrapolated values evaluated with Richardson extrapolation method.

coolant outlets. Due to the great difference in terms of width between equatorial port and gap, it becomes important to set up a simulation in which the abrupt area contraction experienced by air is studied. In particular, It has been investigated the agreement in terms of Nu number between the present setup and the previous (see section 3.1), together with the analysis of the contraction coefficient related to sudden area modification pressure losses.

The initial 3D domain has been halved because equatorial port is symmetric with respect to the vertical plane which halves the BB segment. Starting from this 3D configuration, shown in figure 3.6, 2D domain (shown in figure 3.7) has been extracted, since it is not necessary to study the whole vertical extension of the port to get an overall view of the problem. Gap position is shifted with respect to the equatorial port middle plane because of the design geometry of the OB BB segment, which is divided in three section [20] [21].

The simulation setup is strictly related to the previous analysed case. The selected boundary conditions are:

- *Velocity inlet*: constant velocity specified at inlet, with values set up in order to keep the same mass flow rates tested before (note that it is also possible to specify directly the mass flow rate value though *Mass flow inlet* boundary condition);

- *Pressure outlet*: 0 Pa as gauge pressure;

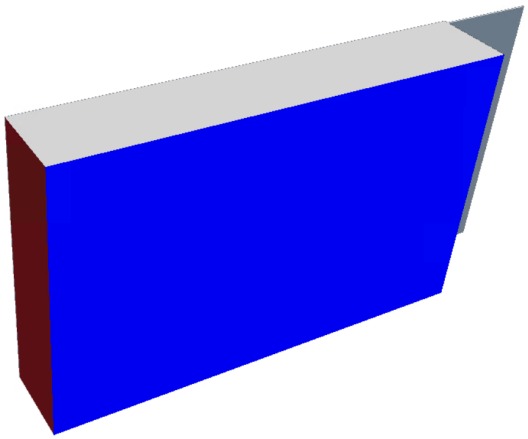

Figure 3.6: 3D domain of the second test case after halving (Blue refers to symmetry plane, Grey refers to walls and Orange represents the fluid inlet).

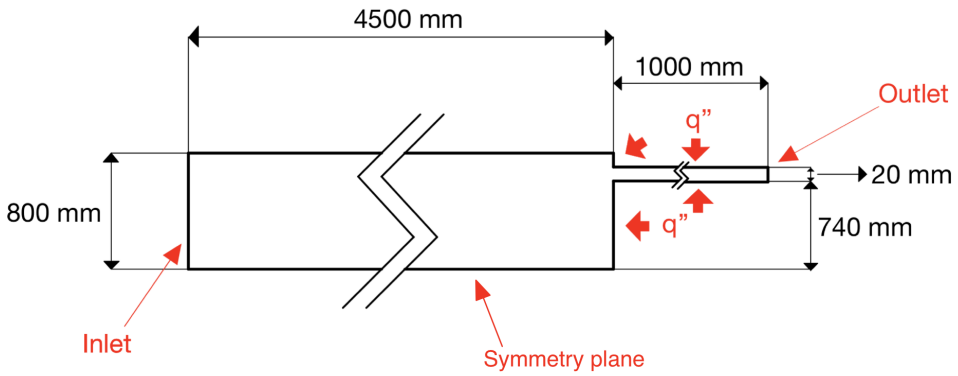

Figure 3.7: Sketch of 2D domain used in STAR-CCM+.

- *Symmetry plane*: used for the halved equatorial port boundary;
- *Adiabatic wall*: used for the other equatorial port surface;
- *Heated wall*: to describe the BB segments adjacent to the gap. Heating is set constant and uniform at $100\,\mathrm{W\,m^{-2}}$.

External environment conditions are 0 Pa (gauge pressure) and 300 K.

Mesh configuration is based on mesh number 2 shown in table 3.1. However, some modifications have been necessary to reduce the cell count. Indeed, the refinement adopted inside the gap is excessive in the equatorial port zone, far from the gap, where the air is free to flow in a wide space and there are no obstacles through which turbulence comes out. *Custom controls* have been switched on: this options allow to change mesh parameters at selected surfaces (*Surface control*) or in a precise domain area/volume *Volumetric control*. Two *Surface control* have been used to reduce mesh refinement at air inlet and the symmetry plane boundary. After the adjustment, new target surface cell size is 0.3 m for air inlet boundary, 0.7 m for the other. In practise, mesh cells of these boundaries do not have all the same prescribed dimension, because several characteristics must be taken into account by the software mesh generator, but it changes the grid to satisfy as much as possible also the presence of *Custom controls*. Figure 3.8 shows the final results after adjustments: it is clearly visible the coarser part close to symmetry plane and inlet, which progressively becomes finer close to the gap.

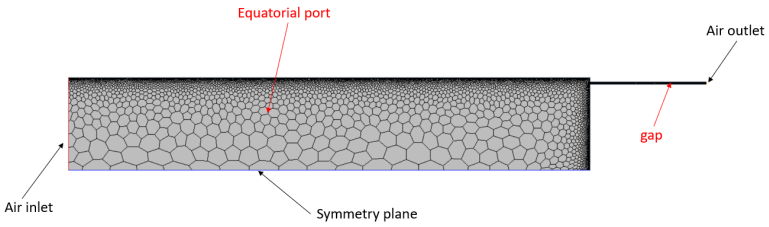

Figure 3.8: Port and gap mesh scene with some annotations: Boundary Conditions in black, domain areas in red.

Nusselt number is evaluated at the outlet of the gap, in agreement with the previous case, but here the gap is only 1 meter long to be consistent with the real design. The agreement of Nusselt number calculation between the two validation cases is shown in figure 3.9, where is clear the similarity in all the investigated Reynolds Number interval. This result is important because it represents a countercheck of the previous computation, giving reliability to the setup selected for the simulation.

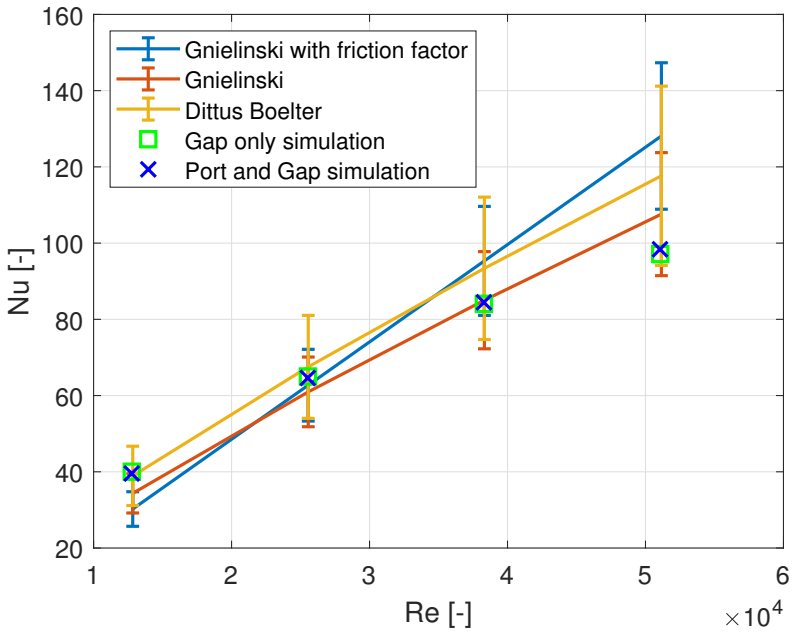

Figure 3.9: Computed Nusselt values compared with correlations available in literature.

The other parameter used to ensure the simulation setup goodness is the contraction coefficient which refers to localized pressure drops. It has been included because it is both easy to calculate in the simulation and experimentally measure (at least in simple configurations), therefore provides a benchmark to evaluate the goodness of simulation strategy. Contraction coefficient has been evaluated in the simulations according to equation 3.15 [27].

$$K_{loc} = \frac{2(p_1 - p_3)}{\rho v_3^2} + \left(\frac{v_1}{v_3}\right)^2 - 1 \tag{3.15}$$

Coordinates where to locate point 1 and 3 have been selected taking into account pressure behaviour along the domain. $x = 2m$ corresponds to subscript 1 and it is the unperturbed upstream location with respect to the sudden contraction. $x = 4.7m$ is the coordinate for point 3 and it is one of first downstream locations with pressure values not influenced by the presence of recirculation areas in the flow. The above mentioned coordinates are highlighted with a cross in figure 3.10. This seems to be the best choice, because further downstream it would become not negligible the contribution of friction inside the gap, bringing to an overestimation of the localized pressure drop coefficient.

Figure 3.10 shows an example of pressure profile all along the investigated domain, clarifying the choice of the coordinate where to calculate pressures and

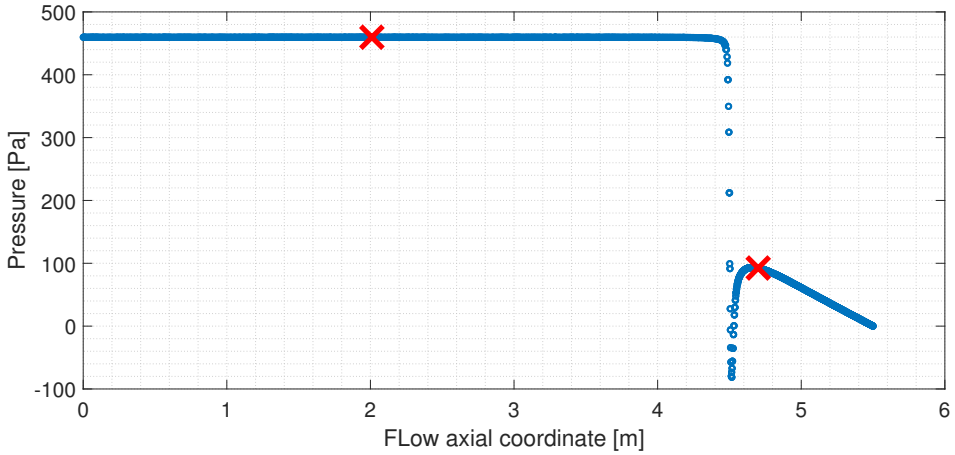

Figure 3.10: Gauge pressure measured on a plane parallel to flow direction, placed in the middle of the gap ($Re = 5 \cdot 10^4$); Red crosses point out the selected location to evaluate contraction coefficient.

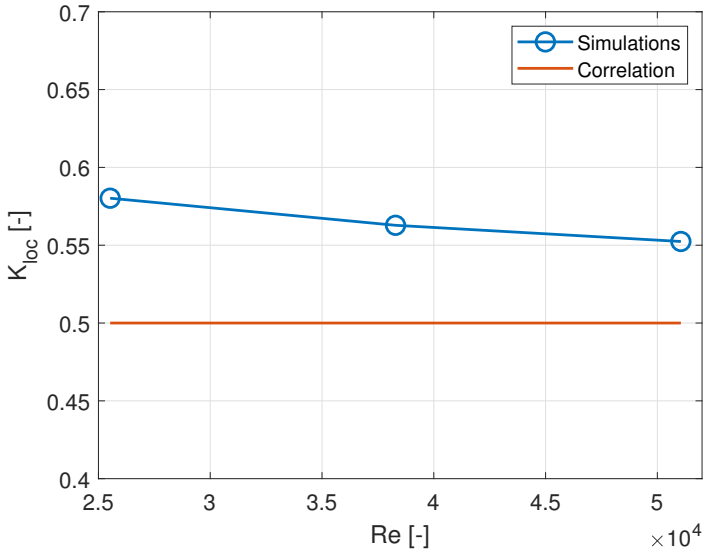

Figure 3.11: Contraction coefficient calculated for different Re compared with theoretical value.

velocities. All the quantities are computed through surface average on planes perpendicular to the flow. Density is the only constant value (due to the adopted physical models).Figure 3.11 shows the contraction coefficient evaluated at different Reynolds number, compared with the prescribed value of 0.5. Despite the rather good agreement between the two, it must be underlined that they are not

easily comparable. Indeed, the theoretical 0.5 value is the contraction coefficient for sharp-edged entrance region given for circular tubes with symmetric contraction [27], whereas the validation case foresees a rectangular duct with asymmetric contraction. Consequently, the reliability of this validation case has been further assessed with another simulation. Here the gap has been shifted to make it symmetric with respect to the equatorial port. However, the overall simulation setup (boundary conditions, meshing parameters, contraction coefficient calculation strategy) is completely equal to the asymmetric-gap case. Figure 3.12 shows

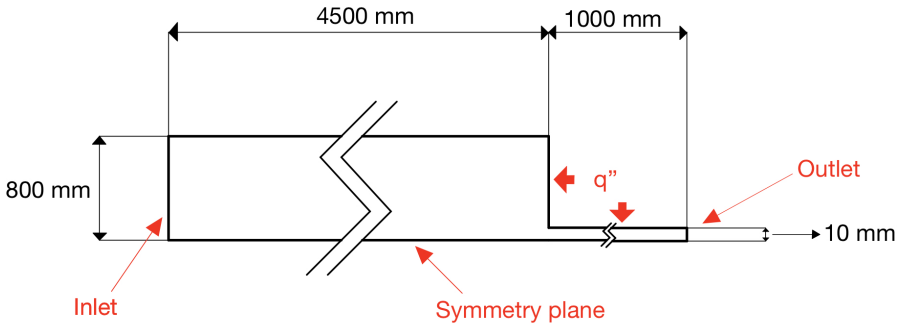

Figure 3.12: Geometry of the simulation with gap symmetric with respect to equatorial port.

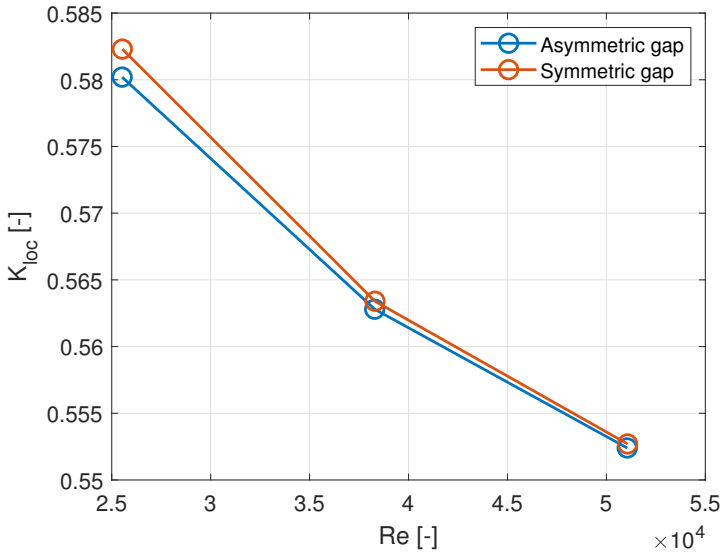

Figure 3.13: Comparison of contraction coefficients obtained in the two simulations.

the detailed geometry of the symmetric gap simulation whereas in figure 3.13 are visible the results of the contraction coefficient comparison between the two simulations. The strong similarity between computed K_{loc} gives the sought reliability to the setup adopted firstly in the asymmetric case.

3.3 Three dimensional turbulent simulation

The 3D turbulent setup is necessary to study the second cooling option proposed to cool down IVCs. In this case, air will be actively introduced in the vacuum chamber through the equatorial port, thanks to a venting system. Equatorial port has been chosen due to lack of space in the other two VV openings: cryopumps are in correspondence of the lower port and upper port should be occupied by remote maintenance systems and other machine piping. However, it is not excluded other air inlet options (expecially the upper port) will be investigated in the future. Regardless the air inlet, active cooling solution is taken into account because it should reduce significantly the cooling time to reach RH requirements, exploiting forced convection and turbulence.

The simulation reference geometry is again the EU DEMO 2017 baseline ([20], [21]), therefore the modelling strategy remains the same: detailed discretization applied just on the maintained sector, symmetry exploitation with respect to vertical plane which crosses the mentioned sector in the middle. WCLL decay heat and thermophysical properties are equal to natural convection case (see sections 2.1 and 2.2) Apart from the equatorial port, now set up as *Velocity inlet*, the other boundary (and initial) conditions are in agreement with natural convection case, since the vacuum chamber environment is the same (see figure 3.14). Being in a really preliminary phase of IVCs cooling strategies study, air flow rate through equatorial port is still unknown. For this investigation it has been assumed 10 $\mathrm{kg\,s^{-1}}$, leading to 1.885 $\mathrm{m\,s^{-1}}$ port inlet velocity (see equation 3.16), considered constant over all the port cross area. A $\sim 2 \cdot 10^3$ Pa pressure drop through the machine was expected (and confirmed by the simulation) in this configuration.

$$v_{inlet} = \frac{\dot{m}}{\rho A_{cross}} = \frac{10\mathrm{kg\,s^{-1}}}{1.18415\mathrm{kg\,m^{-3}} \cdot (1.6\mathrm{m} \cdot 2.8\mathrm{m})} = 1.885\mathrm{m\,s^{-1}} \tag{3.16}$$

3.3.1 Mesh configuration and Time Scales

The problem keeps to be multiscale in space and time, solved with partial decoupling of the time scales already adopted in natural convection case. The difference between time scales is the same, being the fluid time scale $\frac{1}{10}$ of the solid one. *Polyheadral mesher* and *Prism Layer mesher* have been used in agreement with the simplified cases investigation. Indeed, as confirmed by STAR CCM+ user

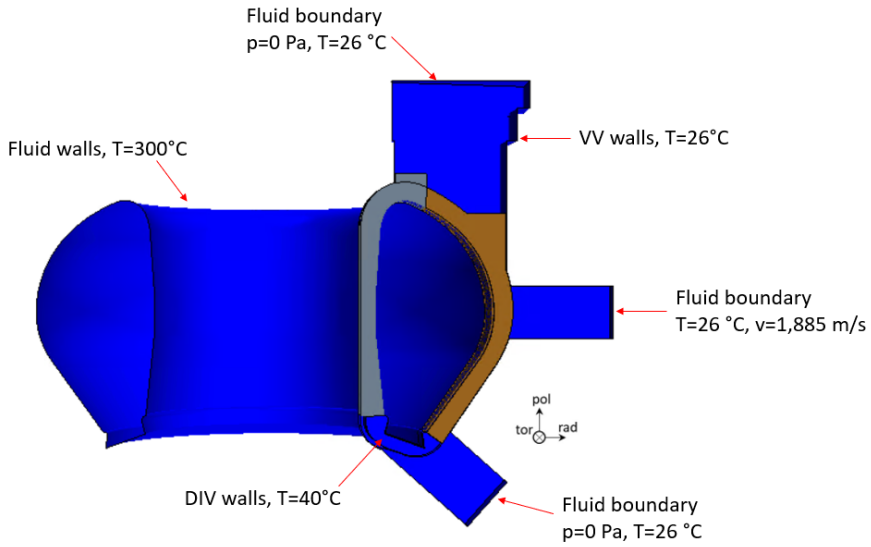

Figure 3.14: Computational domain including the boundary conditions. Fluid domain surfaces are blue, IB segment grey and OB segment brown.

manual, polyhedral meshes provide a balanced solution for complex mesh generation problems. They are relatively easy and efficient to build and also contain approximately five times fewer cells than a tetrahedral mesh for a given surface [22]. Due to the limited computational resources, it was not easy to perform meshing procedures for such a domain: the expected overall cell count was at least one order of magnitude higher than natural convection case and expectations have been confirmed by the execution. When one has to deal with millions of cells, only the meshing procedure can last several hours and it becomes complex to find a good solution in reasonable time. Table 3.2 summarizes the main characteristic of the final mesh setup. The overall cell count of this configuration is $\sim$ 29 Million cells. Similar setups with 10 and 15 Prism Layers count, respectively, $\sim$ 44 and $\sim$ 66 Million cells. Being the first attempt to simulate the forced convection cooling of IVCs, the 5 Prism Layer configuration has been preferred, since the mesh complexity is already rather high. Even if the Base Size has been lowered with respect to natural convection configuration (0.5m), the Target Surface Size ensures that, where possible, bigger cells are created. Prism Layer Total Thickness value is not related to Base Size but it is an absolute value, in order to be suitable for 2cm thick gaps. Prism Layer Near Wall thickness value ensures progressively thicker prism layer from the surface towards the core mesh. Two Custom Control have been added to reduce the overall cell count: One disables the Prism Layer creation on the surfaces belonging to solid segments, the other reduce the mesh

refinement far from the maintained sector via volumetric control (see figures 3.15 and 3.17). About 19 Million out of $\sim$ 29 belongs to fluid domain, $\sim$ 4.8 belongs to IB segment and $\sim$ 5.2 are located in OB segment. As expected, fluid gaps with Prism Layers bring the most important contribution to the overall cells count.

Table 3.2: Main parameters of the mesh adopted in 3D turbulent simulation.

Parameter	*Value*
Base Size	0.1 m
Target Surface Size	250% of Base Size
Minimum Surface Size	5% of Base Size
Surface Growth Rate	1.3
Number of Prism Layers	5
Prism Layer Total Thickness	4 mm
Prism Layer Near Wall Thickness	0.02 mm

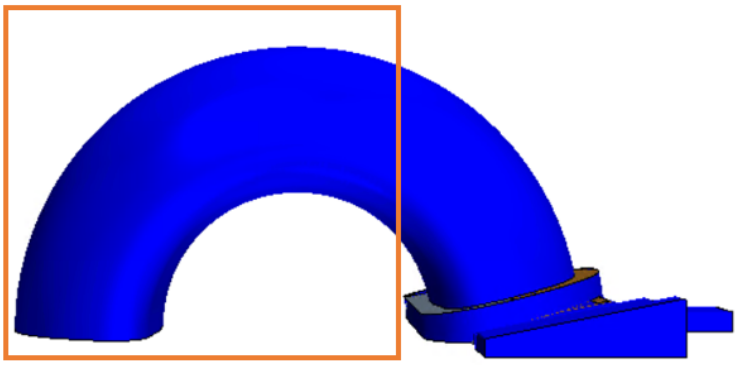

Figure 3.15: Top view of the domain where is shown the part of volume at which Volumetric Control has been applied (inside red box).

Figure 3.16 shows two overall views of the mesh. Figure 3.17 gives an idea about prism layers incidence and shows the effect of the volumetric control in the bottom left view, with a progressively increasing cells dimension in the plasma chamber far from the maintained sector (the reference cell dimension imposed by volumetric control is 1m). The presence of volumetric control is not visible in Figure 3.16 because it does not act on the external surface but just inside the domain. Figure 3.18 details the 3D aspect of the fluid domain mesh inside gaps, very fine also far from corners and edges because the gap thickness is always the same. On the other

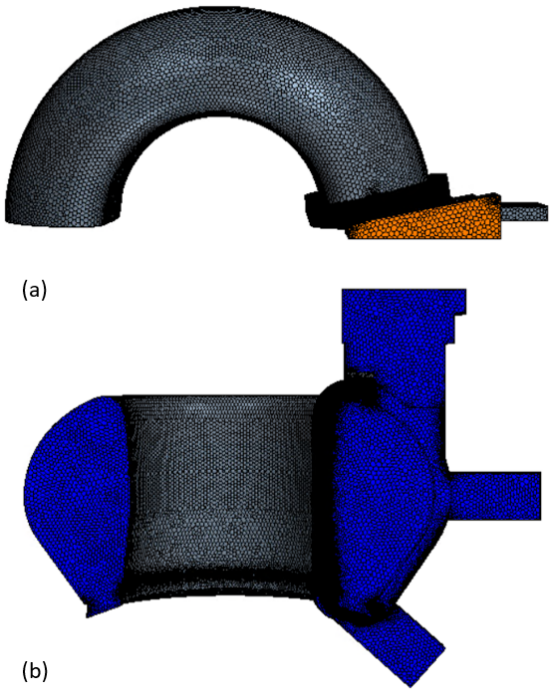

Figure 3.16: Top view (a) and Front view (b) of the complete 3D turbulent mesh.

hand, bigger and progressively increasing cells are visible in the upper port area. Even Prism Layers, being a core solution, are not visible from external surfaces (figure 3.16 and 3.18) but just from cut views as in figure 3.17. Even if the above mentioned meshing setup has been validated through simpler cases and seems to work properly, it does not represent the only solution available. Due to the number of parameters involved, other choices could get a better trade-off between computational cost and obtained results. However, the investigation needed to further improve the mesh could be itself excessively time-consuming to be performed.

3.3.2 Models and Solvers

Solid models are equal to the natural convection case because they are not affected by the higher degree of complexity of forced convection. The presence of turbulent flow, at least inside gaps, where highest velocities are reached, is faced with a turbulence model. In agreement with the simplified setups, the simulation exploits k-Omega-SST turbulence model. Segregated flow model has been preferred to the coupled: it ensures higher convergence ease and there was no need to use a coupled approach without a compressible flow and/or buoyancy forces. Consequently, Segregated fluid temperature model solves the energy equation. Im-

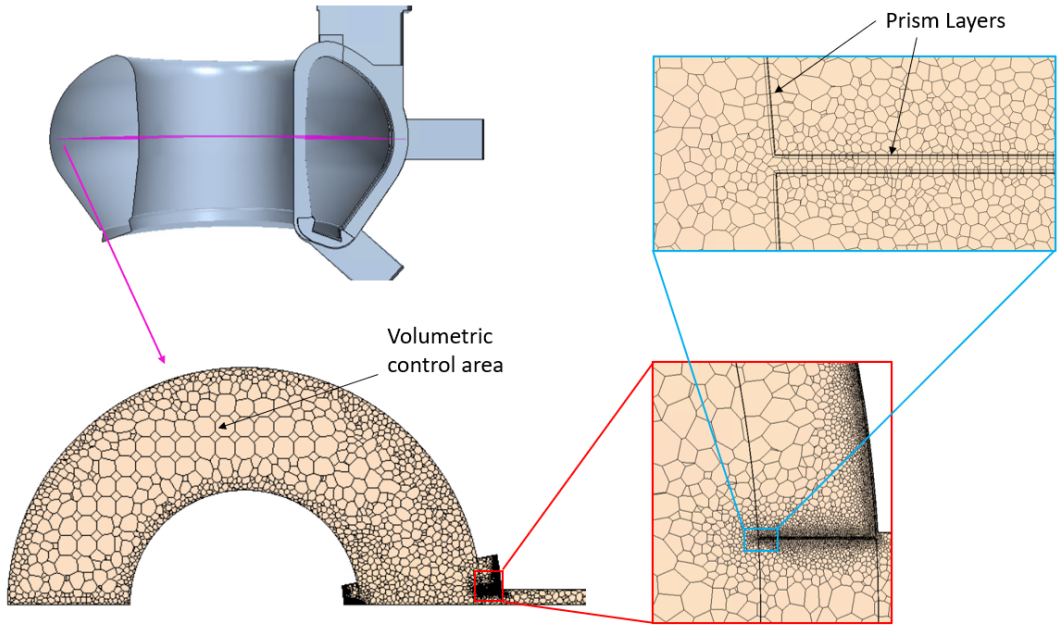

Figure 3.17: 3D turbulent mesh: focus on Prism Layers through an horizontal plane crossing the domain in the middle.

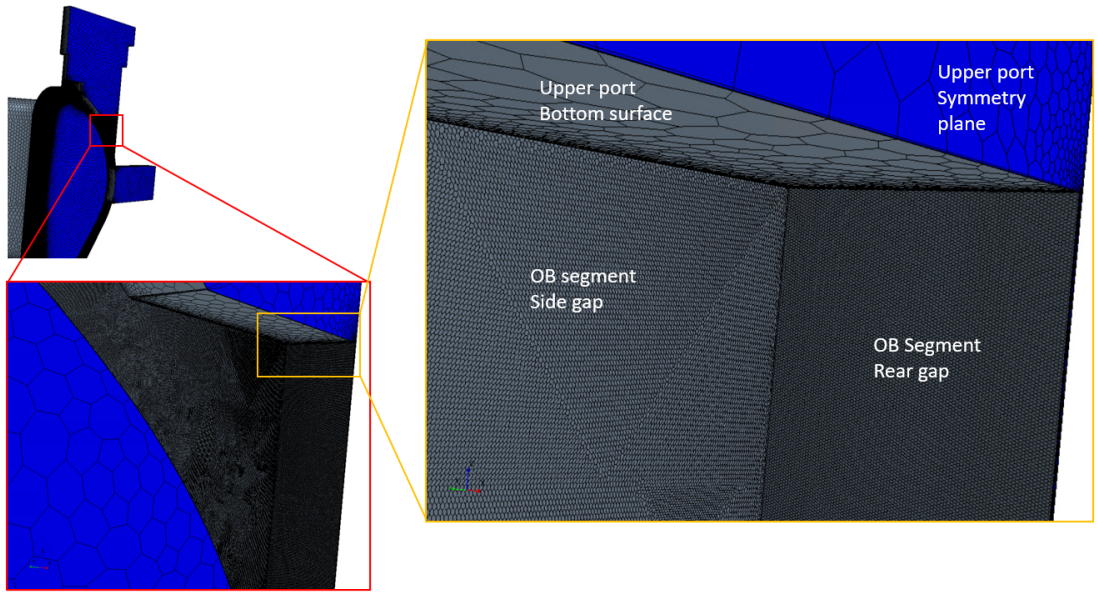

Figure 3.18: 3D fluid domain mesh view with a progressively increasing zoom to give an idea about the cells dimension difference between gaps and wider areas.

plicit unsteady is the time model as in natural convection case. Fluid equation is solved via 'Constant density' model, without taking into account the presence of Buoyancy. Indeed, as mentioned in section 3.1, the calculation of Gr/Re^2 adimensional group suggests a strong prevalence of forced convection inside gaps. For this reason, together with the attempt to reduce as much as possible the model complexity, buoyancy has not been included.

3.3.3 Results

Figure 3.19 gives an overview of the segments maximum temperature evolution in time. The IB cooling time has been predicted with double exponential fitting, due to the lack of time to finish the simulation. The forced convection cooling results immediately far more efficient than natural convection. The OB segment maximum temperature goes under 150°C after less than 26 hours, whereas IB segment goes below the threshold after more than 460, (∼19 days) (see figure 3.19a). This is an important result if compared with the previous investigated case: OB segment cooling time is ∼200 times lower, whereas IB segment ∼20 (see table 3.3). Notice that the cooling time reduction are useful to give a rough

Table 3.3: Solid segments cooling time to reach 150°C.

	Natural convection cooling	*Forced convection cooling*	*Reduction produced by forced convection*
OB segment	220 days	26 hours	∼200 times lower
IB segment	350 days	19 days	∼20 times lower

comparison between the two strategies, since they are calculated with some cooling time extrapolated values. The temperature decreases exponentially because of the heat transfer effectiveness reduction. Moreover, the simulation reveals that the solid average temperature tends to reach an asymptotic average temperature close to 95°C. Once reached the asymptotic temperature (after ∼60 hours of transient), there is a further deterioration in the heat transfer. This behaviour is clearly visible in the IB segment maximum temperature evolution: it takes about 60 hours to reach 165°C, other 400 to reach 150°C. In agreement with the shorter cooling time, the segments heating by decay heat is lower. Starting from 300 °C, the IB segment reaches just some tens of degree over 302°C and the heating lasts about 1.5 hours (see figure 3.19b). As in all the other investigated cases (natural convection of WCLL BB and HCPB BB), the decay heat heating has a negligible effect with respect to the whole transient evolution.

As said, remote handling equipment should grab the segments from the upper port. It becomes quite relevant to have information about the temperature

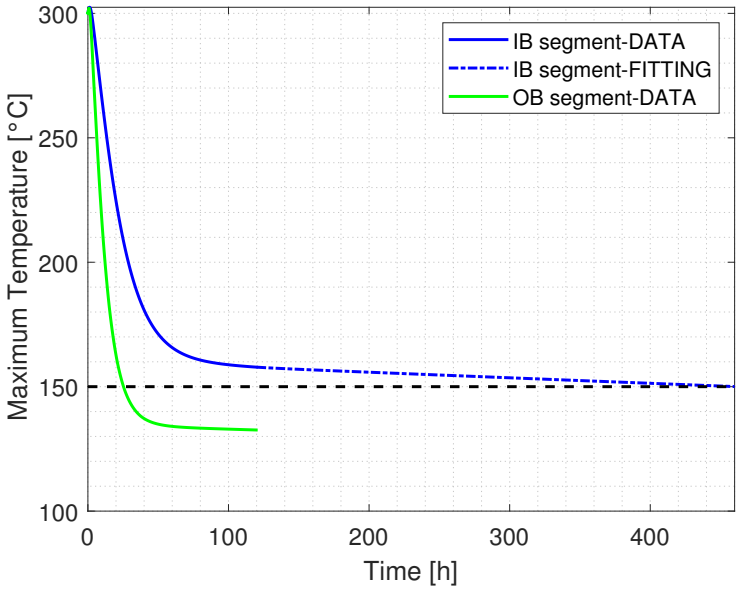

(a)

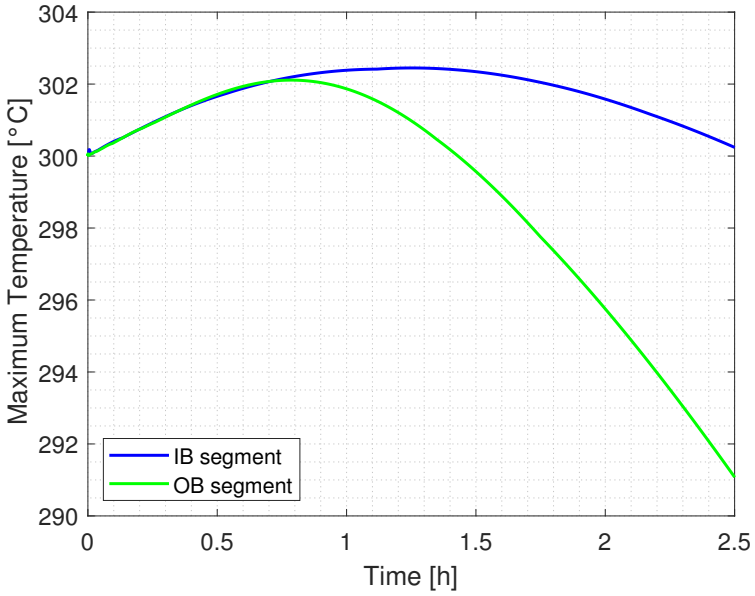

(b)

Figure 3.19: Solid segments and fluid domain maximum temperature evolution in time; Figure (a) gives a view over the whole transient, with the horizontal dashed line to highlight the 150°C threshold; Figure (b) gives a focus on the first hours of the transient, where solid maximum temperatures rise due to the decay heat; Note that both temperature and time scales are different.

evolution on the surfaces on which it will be attached the RH machine. Indeed, the procedures could start even if the overall segment temperature is not under 150°C, provided that the surface of interest is. Figure 3.20 shows the surfaces on which the RH system should be anchored. Surface average temperature on them has been monitored to understand if the RH equipment should be set up even before the end of the whole segment cooling. The average OB segment RH surface temperature goes under 150°C after ∼9 hours and below 130°C after ∼13 hours. Even if there is no information about the maximum temperature on this surface, it is reasonable to think that the procedure to bring RH system in position should start before the ∼26 hours to reach the whole OB segment cooling. However,it must be taken into account that these considerations are useful only if the OB segment will be removed first, but at present it is still unknown what will be the precise RH work schedule. Concerning IB segment, the result is even more interesting: RH surface average temperature is ∼140°C after ∼30 hours and ∼126°C after ∼45 hours. Again, if the IB segment will be removed first, it is very likely the RH procedures could start much earlier than the ∼19 days required to cool down the whole segment.

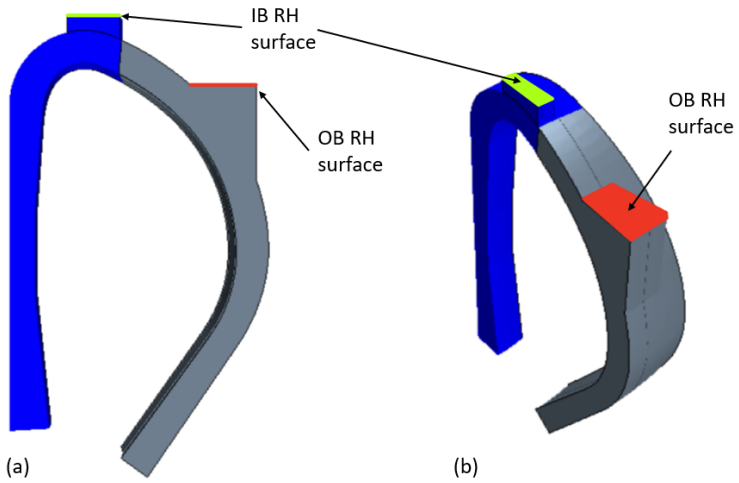

Figure 3.20: 2D front view (a) and 3D view (b) of half of the maintained segments (IB in blue, OB in grey); In red is shown the OB segment RH surface, in green the IB segment RH surface.

In figure 3.21 is visible the motion field of the air inside the plasma chamber, 4 hours after the transient beginning. Again, several differences with respect to the natural convection case are clearly visible. First of all, the air velocity goes up to $\sim 45\,\mathrm{m\,s^{-1}}$, one order of magnitude higher than the correspondent value in natural convection case. The flow comes from the equatorial port, therefore the

highest velocities are located at OB segment gap(see figure 3.21a), right after the abrupt cross area reduction. There is a quite homogeneous distribution of the flow between upper and lower part of the chamber, $\sim 58\%$ of the total inserted mass flow rate goes out from the upper port, $\sim 42\%$ from the lower. This difference is reasonably due to the geometry of the machine (it cannot be justified by buoyancy, not added to the model), indeed the flow towards the lower port must cross the divertor and make stronger curvature. As shown by the cooling time data, the IB segment cooling is less effective, because the air has to cross all the plasma chamber to get to it. Moreover, once arrived, it has already been heated up by the OB segment and its velocity is lower, causing a reduction in the heat transfer efficiency. Figure 3.21b shows the lower extent of air velocity inside IB segment gap (which is located at domain symmetry plane). It highlights also the difficulty of the air to reach the upper port, due to the presence of the IB segment anchoring device which closes the IB segment gap and forces the air to go through the OB gap to leave the plasma chamber. Recirculation phenomena are present in the middle of the plasma chamber and in correspondence of the two outlet port, especially visible in the upper one.

The mass flow rate distribution inside the chamber can be better appreciate in figure 3.22. Figure 3.22a gives an overall view of the path of some selected streamlines from the equatorial port inlet until the domain outlet. Part of the air flow towards the upper port and exits after a recirculation zone. Even this view shows that the warm air coming from the chamber is evacuated by the right portion of the port. On the other hand, the flow towards the lower port comes both from the rear OB gap and from the most IB part of the divertor. Part of the air enters the plasma chamber and flows inside it, towards the non-maintained sectors. For this reason, some streamlines are still visible in the opposite part of the chamber, meaning that part of the air runs through all the plasma chamber before exiting. Figure 3.22b gives a detailed view of the flow splitting at the end of the equatorial port. Part of it goes in the OB segment rear gap, both in the upper and lower directions, and part goes through the OB segment middle gap. The presence of the OB central segment (hidden in this view) causes the deviation of the main flow and it makes more difficult the fluid entrance in the chamber.

Figure 3.23 shows temperature maps at different locations and different time instants during the transient. Because of the equatorial port air inlet, the cooling starts from the OB segment middle part, but the process is really effective in all the segment rear part, thanks to the flow in the rear gap, which is also easily connected with both the outlet ports. As visible in figure 3.23a, 1 hour after the beginning of the process, when almost all the segment has temperature close to 300°C, there is a colder layer(250°C - 200°C) in the rear part of it. A comparison between figures 3.23a and 3.23b, at every time instant, reveal the already mentioned discrepancy in

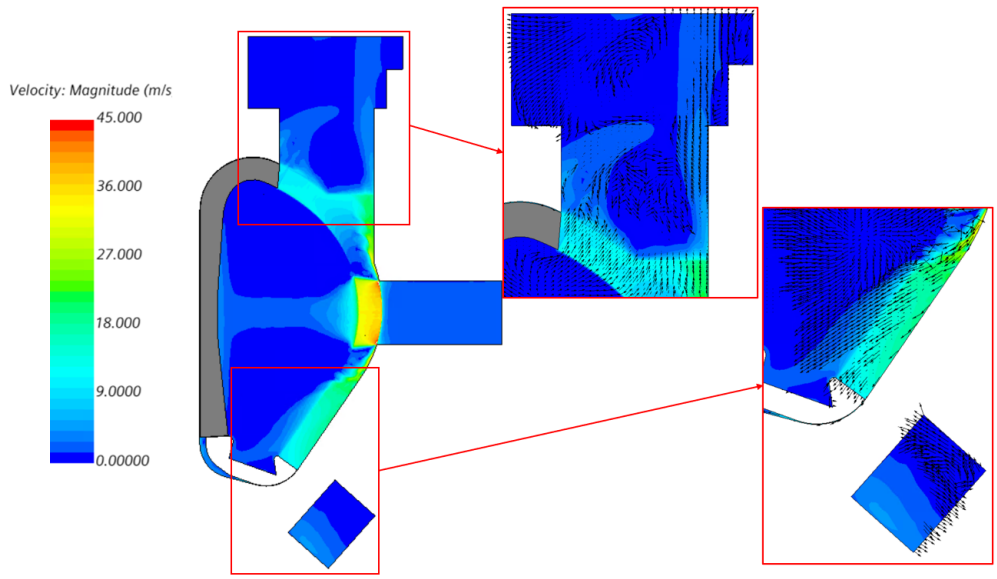

(a) Velocity magnitude in a plane crossing the OB segment gap together with insets of the vectorial field inside the gap and in correspondence of the upper and lower ports; the lower port appears cut because it has a progressively increasing cross area and this plane crosses just part of it.

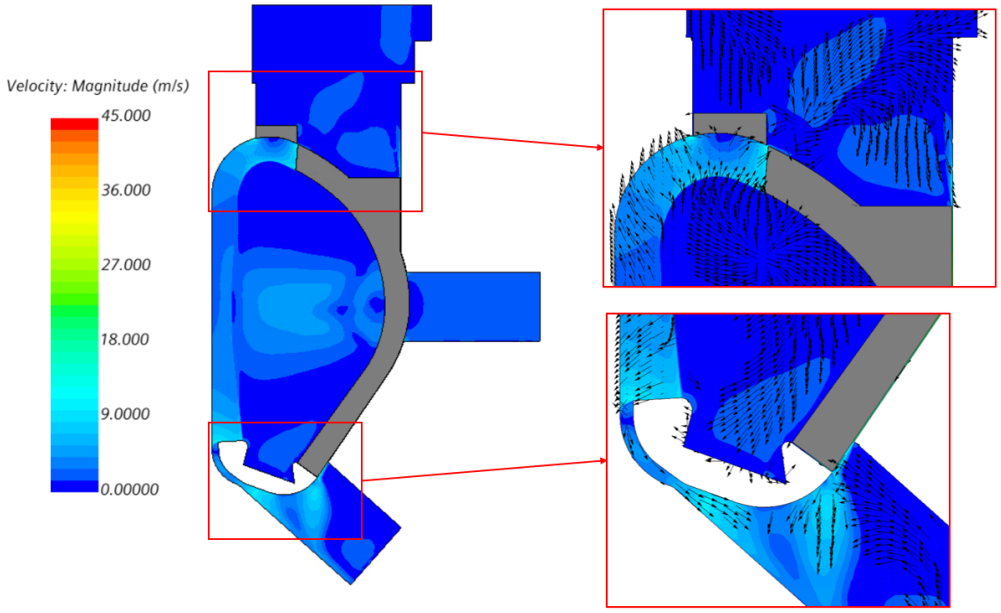

(b) Velocity magnitude at domain symmetry plane together with insets of the vectorial field at plasma chamber top and bottom parts.

Figure 3.21: Motion field at different positions inside the domain, 4 hours after the transient beginning; note that vectors are used just to show the direction of the flow: their length is constant and it does not represent the velocity magnitude.

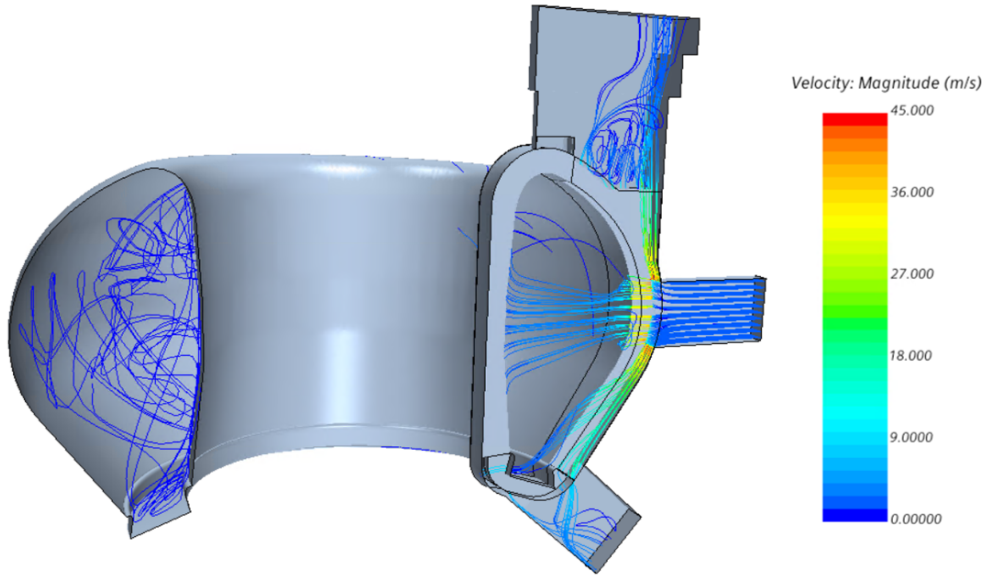

(a)

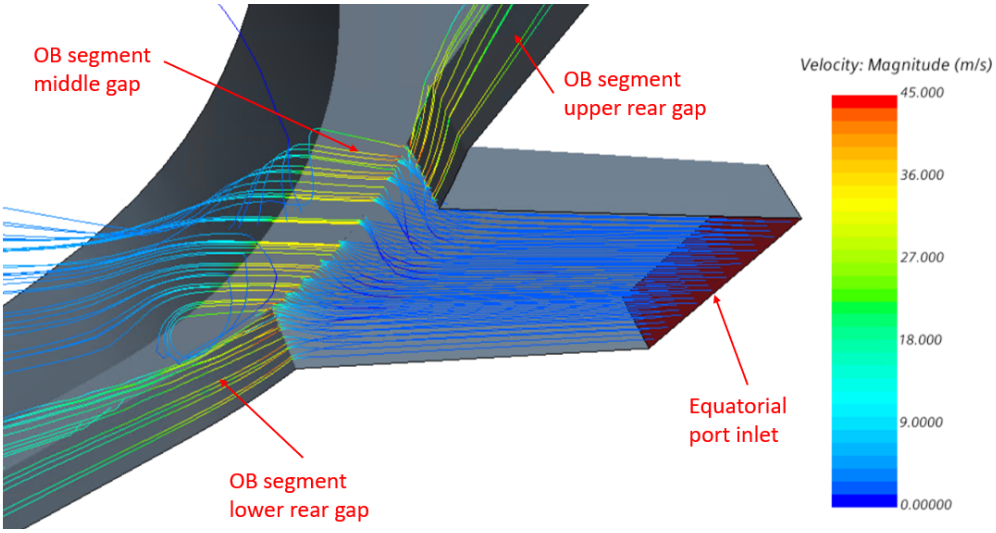

(b)

Figure 3.22: Streamlines 4 hours after the transient beginning in the whole plasma chamber (a) and an detailed view of the equatorial port zone (b); Note that in (b) the central OB segment is hidden to better appreciate the flow inside the OB segment gap.

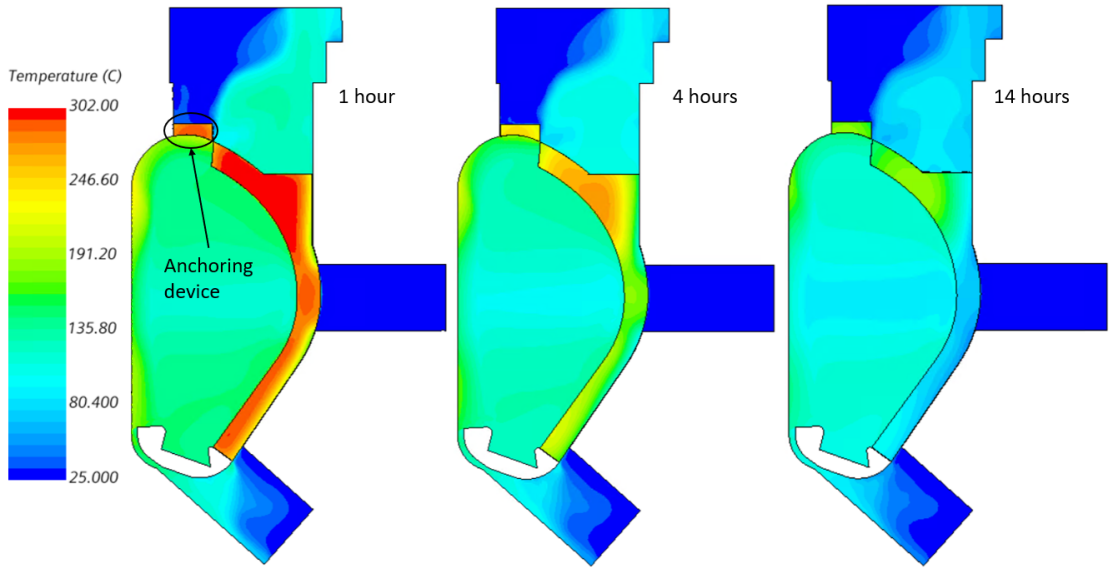

(a) Temperature field at domain symmetry plane, which crosses the IB segment gap and the OB segment solid part.

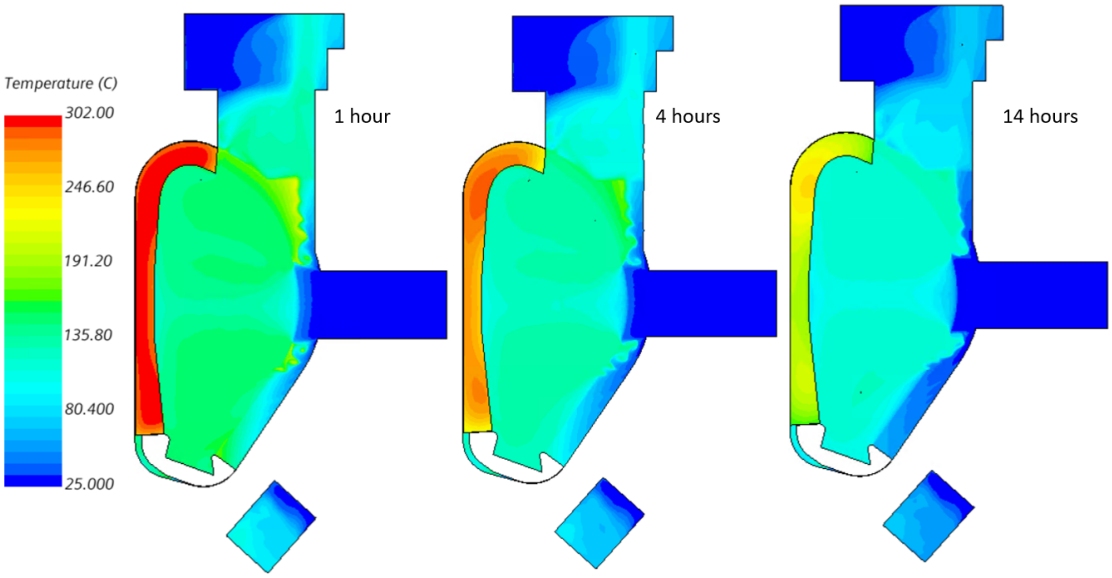

(b) Temperature field in correspondence of OB segment gap, showing temperature inside the IB segment; the lower port appears cut because it has a progressively increasing cross area and this plane crosses just part of it.

Figure 3.23: Temperature field at different sections of the machine, respectively 1, 4 and 14 hours after the beginning of the transient.

segments cooling. For example, after 4 hours, OB segment has already experienced a great drop, with temperature lower than 200°C in its middle zone (see fig. 3.23a), whereas IB segment temperature is still near $\sim$ 250°C (see fig. 3.23b). From these temperature maps is clear the presence of two zones inside the upper port: one warmer region on the right and one colder region on the left. This is the consequence of the above mentioned anchoring device, visible in the symmetry plane cut (figure 3.23a). It blocks the air which flows in the gap between the two IB segments and the air must go in the OB segment gap to reach the upper port. In this way, the heated air flows just in the right part of the upper port and the left is occupied by stagnant ambient temperature air.

Although the transient makes the temperature field always changing in time, this is not true for the motion field. This particular has been fundamental to speed up the simulation. Indeed, exploiting the stationary behaviour assumed (after a first transient period) by the motion field, the fluid momentum and turbulence equations resolution has been frozen to decrease the solution complexity. This operation has been possible thanks to the absence of gravity, which, if present, would have been a temperature dependent thermal driver. In this way, next time steps has been simulated always with the same motion field, whereas the energy equation resolution was still active to catch the temperature evolution. Even the number of inner iteration set up for the fluid domain resolution has been reduced to 1 (starting from 30) because inner iteration were mainly used by the solvers to get better resolution of the whole set of momentum equation. Finally, the fluid time step has been increased up to be equal to the solid one. This combination of adjustments has brought to a $\sim$220 times simulation acceleration. Figure 3.24 shows the agreement between motion field taken at different time instants during the transient.

The above mentioned simulation speed up results to be very useful even because, on the other hand, the goodness of fittings has been confirmed not always reliable. Extrapolations has been used to try to get a good estimate of the cooling time without waiting the end of the simulation. Figure 3.25 shows a plot where the extrapolated OB segment cooling time (CT) has been compared with the value got at the end of the simulation. The plot shows the error of each estimate with respect to the simulated value (see equation 3.17), together with the percentage of simulation at which every fitting has been done. Every fitting uses a double exponential function (see equation 3.18).

$$Error_{estimate} = \frac{|CT_{estimate} - CT_{simulated}|}{CT_{simulated}} \cdot 100 \quad [\%] \tag{3.17}$$

$$f(t) = a \cdot e^{b \cdot t} + c \cdot e^{d \cdot t} \tag{3.18}$$

The error made by fitting the solution decreases with the simulation progress but starts from quite high values ($\sim$37% the maximum, see 3.25).

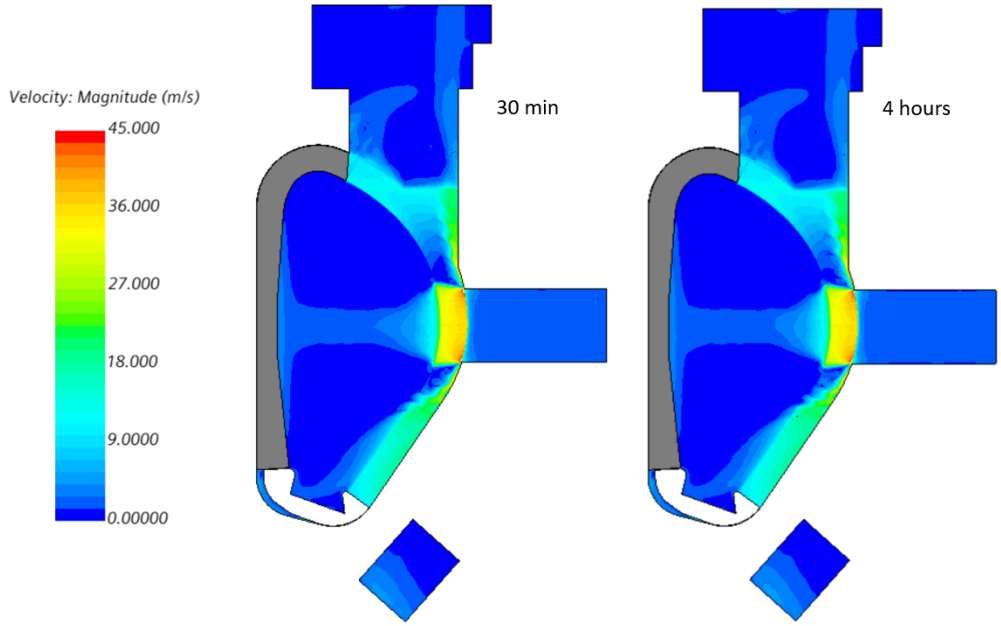

Figure 3.24: Comparison between the motion field over a plane crossing OB segment gap, 30 minutes and 4 hours after the transient beginning. The agreement between the two shows the reached motion stationarity.

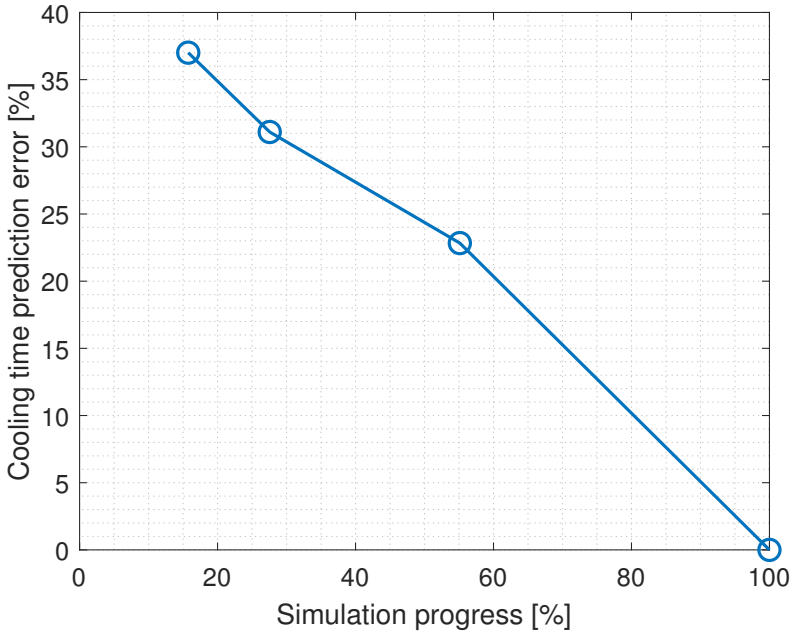

Figure 3.25: Goodness of the IB segment cooling time estimate done after a certain percentage of simulation progress. Simulation progress = 100% means the threshold has been reached (∼26 hours for IB segment).

Moreover, even if it is not visible, the estimate is non-conservative. Indeed, as it occurs in the natural convection case, the heat transfer effectiveness decrease as the time passes by, therefore the estimate is based on a heat transfer process that will deteriorate onwards. Things become even worse with the IB segment cooling estimate, because the heat transfer deterioration after 60 hours leads to errors higher than 100%, if the estimate is done before this event. However, an estimate of the IB segment cooling time has been left to give at least an order of magnitude of the transient duration. Furthermore, it is reasonable to think the concerned estimate will have a low error, provided that it starts after 120 hours, when the segment temperature is already lower than 160 °C. Since the simulation has not reached the 150°C threshold, prediction error of IB segment cooling times have not been included.

Chapter 4

Conclusions and perspective

A 3D transient CFD model has been used to study the natural convection cooling of a sector of the EU DEMO tokamak WCLL BB. The model aims to find the time needed to cool down the sector to allow RH procedures, starting 30 days after shutdown. The natural convection set up foreseen a detailed model of the sector under maintenance, with dedicated treatment of the gaps between the BB segments. The 3D CFD model set up is based on the one developed to study the same problem for HCPB BB (see [13]), with specific modifications to include the new BB concept.

The results show that more than 220 days are necessary to cool down all the OB segments from 300°C to 150°C, the maximum temperature at which the RH can operate. More than 350 days are necessary to completely cool down the IB segments. The great difference with respect to HCPB BB (∼15 days of OB segments, ∼85 days for IB [13]) is mainly due to the decay heat, which is already 5 times higher at the beginning of the transient (1 month after shutdown) and further increases monotonically during the process. Taking into account that the maintenance procedures should last about 6 months, the natural convection cooling is not a viable solution.

The investigation has been moved to analysis of the forced convection cooling of WCLL BB, performed by a fan placed in correspondence of the VV equatorial port. Due to the presence of turbulence, the previous CFD model was not able to correctly simulate the flow. Simple test cases have been studied in order to implement the right meshing strategy and turbulence model inside the simulation. This cooling strategy was found to be far more efficient than the previous: ∼ 26 hours are necessary to cool down the OB segments, ∼460 for the IB one. Moreover, considering just the RH surfaces to grab the segments, the OB reaches 150°C after ∼9 hours and 130°C after ∼13 hours, whereas the IB reaches ∼140°C after ∼30 hours and ∼126°C after ∼45 hours. Regardless the RH procedure (it is still not clear what will be the segment extraction), this result makes the forced convection

from the equatorial port a really promising cooling strategy in case WCLL will be adopted in EU DEMO. It does not seem necessary to investigate the forced convection cooling from the upper port, since it could be difficult to install the fan at the upper port together with the RH equipment and the cooling time found with equatorial port cooling is already quite satisfactory.

In perspective, detailed modelling of the sectors near the maintained one could offer a more realistic simulation of the environment. At present, adjacent sectors are assumed to be at constant temperature (300°C) during the whole cooling transient, neglecting their decay heat contribution that could increase the overall cooling time. Actually, a 3D CFD model with this new characteristics has already been built. Figure 4.1 shows the domain of the model, now able to accurately model 8 of the 16 sectors of DEMO (just 4 are visible due to symmetry exploitation). However, the cell count increase due to the addition of three segments is quite high: concerning natural convection simulation (the only one built so far), the overall cell is ∼5 times higher. Once forced convection is concerned, the increase could be even higher, leading to meshes with hundreds of million cells. Unfortunately, the computational resource to properly manage such a model, are not trivial to find. Coming back to simpler improvements, it radiative effects in-

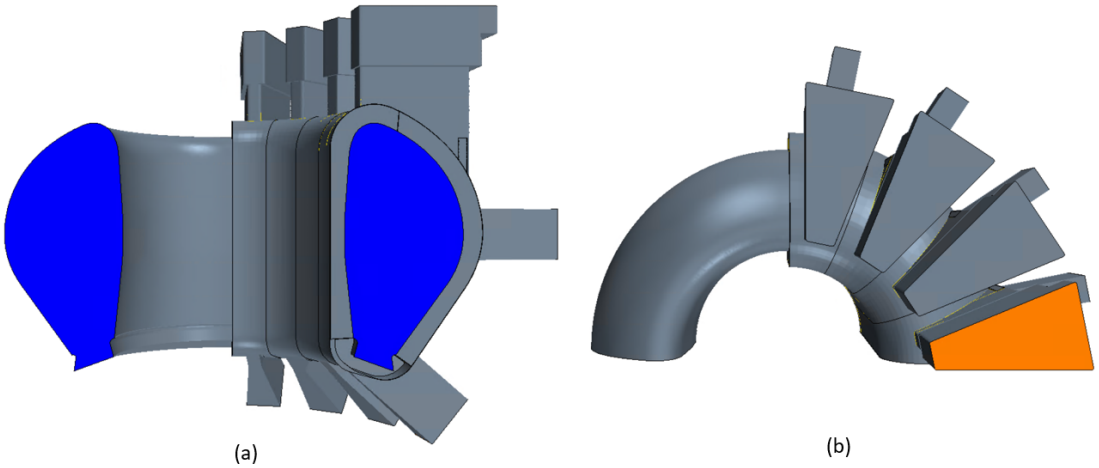

Figure 4.1: Front (a) and top (b) view of the domain used in the simulation with detailed model of the sectors adjacent to the maintained one. In blue is visible the cross-section of the fluid domain inside the plasma chamber, in orange the upper port of the maintained sector, in grey the other domain surfaces.

clusion could be of great interest for the forced convection CFD model, since non negligible temperature differences are present between BB and VV surfaces (respectively 300°C and 40°C at the beginning of the transient). Estimation of the radiative effects impact on BB cooling time will be a good enhancement for the

model. Parametric studies about inlet mass flow rate and inlet air temperature could be useful to reach the best trade-off between cooling time and power of the fan. The same forced convection analysis could than be performed on HCPB BB concept, in order to get an overview of the cooling strategies effectiveness of both the BB concepts.

It would also be important to get more information about the shape and position of prescribed RH surfaces, in order to better isolate them in the reactor CAD model. A detailed study about their cooling evolution could already give a satisfactory evaluation of the adopted cooling strategy, leading to much faster simulations.

Bibliography

[1] Tomas Markovic. "Measurement of Magnetic Fields on GOLEM Tokamak". PhD thesis. June 2013.

[2] ITER organization. *In a few lines*. 2020. URL: `https://www.iter.org/proj/inafewlines` (visited on 09/22/2020).

[3] EUROfusion CONSORTIUM RESEARCH INSTITUTIONS. *The demonstration power plant: DEMO*. 2020. URL: `https://www.euro-fusion.org/` (visited on 09/22/2020).

[4] R. Zanino. *Lecture notes of Nuclear Fusion Reactor Engineering*. NEMO group - Dipartimento di Energia - Politecnico di Torino. A.A. 2019/2020.

[5] Christian Theiler. "Basic Investigation of Turbulent Structures and Blobs of Relevance for Magnetic Fusion Plasmas". PhD thesis. Dec. 2011. DOI: `10.5075/epfl-thesis-5228`.

[6] L. V. Boccaccini. *Lecture notes of Nuclear Fusion Reactor Engineering*. presented at Politecnico di Torino. 2015.

[7] Francisco A. Hernández et al. "Overview of the HCPB Research Activities in EUROfusion". In: *IEEE TRANSACTIONS ON PLASMA SCIENCE* 46 (2019).

[8] A. Del Nevo et al. "Recent progress in developing a feasible and integrated conceptual design of the WCLL BB in EUROfusion project". In: *Fusion Engineering and Design* 146 (2019), pp. 1805–1809.

[9] E. Martelli et al. "Study of EU DEMO WCLL breeding blanket and primary heat transfer system integration". In: *Fusion Engineering and Design* 136 (2018), pp. 828–833.

[10] D. Maisonnier et al. "The European Power Plant Conceptual Study". In: *Fusion Engineering and Design* 75–79 (2005), pp. 1173–1179.

[11] M. Coleman et al. "Concept for a vertical maintenance remote handling system for multi module blanket segments in DEMO". In: *Fusion Engineering and Design* 89 (2014), pp. 2347–2351.

[12] G. Keech et al. “Issues of the vertical blanket segment architecture in DEMO: Current progress and resolution strategies”. In: *Fusion Engineering and Design* 146 (2019), pp. 1408–1412.

[13] A. Zappatore et al. “CFD analysis of natural convection cooling of the in-vessel components during a shutdown of the EU DEMO fusion reactor”. In: *Fusion Engineering and Design* 165 (2021).

[14] Andrea Zappatore et al. *Assessment of natural convection in the plasma chamber and IVC temperatures in non-operating states*. EFDA_D_2MZGBY. 2020.

[15] A. Del Nevo et al. *WCLL BB design and Integration studies 2019 activities*. EFDA_D_2P5NE5. 2020.

[16] Ferenc Gillemot et al. *Material Property Handbook on EUROFER97(2015-MTA)*. EFDA_D-2MRP77. 2016.

[17] Magnus Holmgren. *X Steam, Thermodynamic properties of water and steam*. 2020. URL: `https://it.mathworks.com/matlabcentral/fileexchange/9817-x-steam-thermodynamic-properties-of-water-and-steam` (visited on 09/22/2020).

[18] Engineering ToolBox. *Nitrogen - Thermal Conductivity*. 2018. URL: `https://www.engineeringtoolbox.com/nitrogen-N2-thermal-conductivity-temperature-pressure-d_2084.html` (visited on 09/17/2020).

[19] Tom Berry and Tim Eade. *Calculation of decay heat in PbLi for entire WCLL reactor*. EFDA_D_2NQL5P. 2020.

[20] R. Wenninger. *DEMO1 Reference Design – 2017 March (EU DEMO1 2017)*. EFDA_D_2NE9JA. 2017.

[21] A. Gliss. *June-2017 DEMO Reference Configuration model*. EFDA_D_2N4EZW. 2017.

[22] Siemens PLM Software. *Star-CCM+ User's Manual v14.06*.

[23] J.H. Ferzinger and M. Peric. *Computational Methods for Fluid Dynamics*. 3rd ed. Springer, 2002.

[24] F. Incropera and D. Dewitt. *Introduction to Heat Transfer, 6t̂h edition*. USA: John Wiley & Sons, 2006.

[25] Niel E. Todreas and Mujid S. Kazimi. *Nuclear System*. 2nd ed. CRC Press, 2012.

[26] A. Mansour and E. Laurien. “Numerical error analysis for three-dimensional CFD simulations in the two room model containment THAI+: Grid convergence index, wall treatment error and scalability tests”. In: *Nuclear Engineering and Design* 326 (2018), pp. 220–233.

[27] Bruce R. Munson and other. *Fundamentals of Fluid Mechanics*. 7th ed. John Wiley & Sons, 2013.